FFI Norwegian Defence Research Establishment

22/02062

FFI-RAPPORT

Aspects of Underwater Explosions and Preliminary Modeling in Impetus

Martin Fonnum Jakobsen

Aspects of Underwater Explosions and Preliminary Modeling in Impetus

Martin Fonnum Jakobsen

Norwegian Defence Research Establishment (FFI) 17 November 2022

Keywords
Undervannssprengning
Eksplosiver
Detonasjon
Trykkbølger
Fluidmekanikk
Fluiddynamikk

FFI report
22/02062

Project number
1581

Electronic ISBN
978-82-464-3442-1

Approvers
Morten Huseby, *Research Manager*
Halvor Ajer, *Research Director*

The document is electronically approved and therefore has no handwritten signature.

Summary

The subject of this report, is the physics of underwater explosions (undex). The report has several goals:

- Develop FFI's basic knowledge of undex phenomena as part of the project "1581, Våpenvirkningsmekanikk".
- Provide a general resource for any researcher interested in learning more about undex.
- Perform preliminary undex simulations in Impetus to evaluate its current simulation capabilities.
- Provide concrete benchmarks for the Impetus team in order to improve the code.

The first part (Chapters 2–4) of the report is a detailed literature study of several important undex phenomena, which are useful for benchmarking purposes. In the second part (Chapter 5) we describe our attempts at modeling undex with the numerical code Impetus. Given that Impetus was not designed with undex phenomena in mind, the simulation capabilities are beyond what could reasonably be expected. Impetus is able to describe both the bubble dynamics and shock wave propagation qualitatively, although quantitatively there are still some discrepancies. However, it seems likely that these shortcomings can be overcome with updates to the Impetus code. A range of such improvements are suggested.

Sammendrag

Denne rapporten omhandler fysikken som ligger til grunn for fenomener assosiert med undervannseksplosjoner (undex). Rapporten har flere mål:

- Forbedre FFIs grunnkunnskap om undex-fenomener, som ledd i prosjektet ”1581, Våpenvirkningsmekanikk”.
- Fungere som en generell ressurs for enhver som ønsker å lære mer om undex.
- Dokumentere resultatene av innledende undex-simuleringer i Impetus, og evaluere dets kapabilitet til å modellere den relevante fysikken.
- Dokumentere konkrete eksperimentelle data og teoretiske fysiske formler, som vil hjelpe impetusutviklerne med å forbedre programvaren.

Rapportens første del (kapittel 2–4) er et detaljert litteraturstudium av undex-fenomener. Studiet vil være nyttig for videreutvikling av programvaren. I rapportens andre del (kapittel 5) beskriver vi fenomener vi har forsøkt å modellere i Impetus. Simuleringsresultatene er bedre enn forventet, om en tar i betraktning at Impetus ikke primært er utviklet med tanke på undex-fenomener. Impetus klarer å beskrive både bobledynamikken og sjokkbølgedynamikken kvalitativt korrekt. Det er likevel noen kvantitative avvik mellom simuleringer og eksperimentelle formler. Dersom koden videreutvikles ser det ut til at den kan bli et godt verktøy for å beskrive undex i framtiden. Vi foreslår konkrete utviklingsstrategier.

Contents

1 Introduction

A long term goal at the Norwegian Defence Research Establishment (FFI) is to develop a model that can simulate the physics associated with underwater explosions. A well–functioning model is of importance for the military as well as offshore and subsea industries, because it allows for a description of the loading on structures of interest. The loading mechanisms are important to understand, not only from an attack point of view, but also from a protection point of view. In addition, the removal of WWII naval mines is still a relevant issue in the European coastal waters. To facilitate the safe removal of naval mines, it is necessary to first understand the scale and physical effects of the explosion and then decide on appropriate protection measures.

This report has two goals. Firstly, to provide a detailed reference reviewing important aspects of the physics governing underwater explosions. This will make it easier for any interested researcher to pursue underwater explosions in the future. Secondly, our goal is to investigate well–known undex effects both qualitatively and quantitatively using Impetus, to evaluate its modeling suitability.

In Chapters 2–4, the theory of undex is developed and discussed. There is seen to be a range of both analytical formulas and empirical data for describing important aspects of the physics involved. In Chapter 5 we describe our attempts to perform numerical simulations of relevant undex phenomena using the Impetus code. The simulations are compared with the previously developed analytical theory and empirical data. Based on these comparisons, we discuss whether Impetus is suitable for simulations of this kind and finally provide some suggestions for further development of the code. At the time of writing, this is the first work that attempts to model undex phenomena in Impetus. Therefore, we have focused our modeling efforts on the simplest possible undex phenomena with well–established empirical relations.

2 Physical phenomena of underwater explosions

In general, an underwater explosion (undex) initiates several different physical phenomena that are interesting both from a purely scientific and military point of view. The physics of an undex event can be divided into a shockwave phase and a gas bubble pulsation phase. The two phases are often described independently, because they occur on separate timescales. In the following we concisely summarize these phenomena.

The charge detonation converts the solid explosive material into gaseous reaction products, with an exceedingly large pressure and temperature. The explosion results in a pressure shock wave propagating outwards from the point of detonation. The amplitude of this shock wave is typically several orders of magnitude larger than the amplitude of a similar detonation in air, and the shock can therefore have a considerable effect on structures such as ships or submarines. In general, the net shockwave loading on a structure may consist of three contributions: direct shockwaves, reflected shockwaves from a rigid surface, and reflected rarefaction waves from a free surface. In particular, the rarefaction waves close to the air–water surface can result in local cavitation at the surface. If the cavitation region forms beneath a ship, close to its midsection, the damage may be severe. The underlying reason is that in the cavitation region the water is converted to vapor bubbles which results in a local decrease in buoyancy. Consequently, the ships midsection may literally fall into a crater, while the bow and stern are still floating on water. As shown in Fig. 2.1 (*a*) the situation may cause severe stress on the ships midsection.

A perhaps less obvious physical phenomena is that the gas produced in the explosion forms a pulsating underwater bubble, acting as a source of secondary pressure waves. Initially, the density and pressure of the gas bubble is much higher than the surrounding water pressure leading to volume expansion. During the expansion the gas pressure eventually becomes smaller than the surrounding water pressure, but due to the high inertia of water the gas continues to expand. A non-negligible portion of the expansion actually occurs while the gas pressure is smaller than the surrounding water pressure. Eventually the expansion comes to a halt, and the gas begins to contract while simultaneously increasing its internal pressure. When the gas pressure again becomes significantly larger than the surrounding water pressure, the gas will expand once again. Under realistic conditions the gas bubble can expand and contract several times, before its energy is depleted. The length and time scale of the bubbles maximum radius and pulsation period is determined by the power of the initial explosive, the depth of detonation, and the potential proximity to surfaces. The pulsating gas bubble is strictly speaking also present in air, leading to secondary shock waves. Yet, due to the small density of air the secondary shock waves and pulsation period is much smaller than in water.

A closely related damage mechanism is the so–called whipping effect, see Fig. 2.1 (*b*). If the underwater explosion occurs under the keel of a ship, the oscillating bubble excites violent and dangerous transverse vibrations, especially if the oscillation frequency matches the ships corresponding resonance frequencies. If the ships girder strength is not sufficient to handle this loading, the ship will be severely damaged. If the bubble is sufficiently close to the ship, the bubble may also physically lift the ships keel, potentially resulting in severe deformation as illustrated in Fig. 2.1 (c).

Gravity introduces a pressure variation from the top to the bottom of the bubble, affecting the bubble shape which in contraction resembles a kidney instead of being spherical. Further, gravity also leads to a buoyancy force pushing the bubble upwards towards the surface (bubble migration). Upwards bubble motion means that water must be pushed out of the way, resulting in a drag

force opposite to the buoyancy force. Consequently, the bubbles upward migration is considerable when the bubble contracts, and minute when the bubble expands. Figure 2.2 summarizes the aforementioned features.

Note that when the pressure variation across the bubble is substantial, the bubbles bottom moves faster than its top. If the bottom catches up with the top before re-expansion, the bubble becomes a torus with a jet flowing through the hole. This phenomenon is referred to as jet formation. The jet velocity may be several kilometers per second and can cause significant damage to a structure, e.g. a ship as illustrated in Fig. 2.1 (*d*).

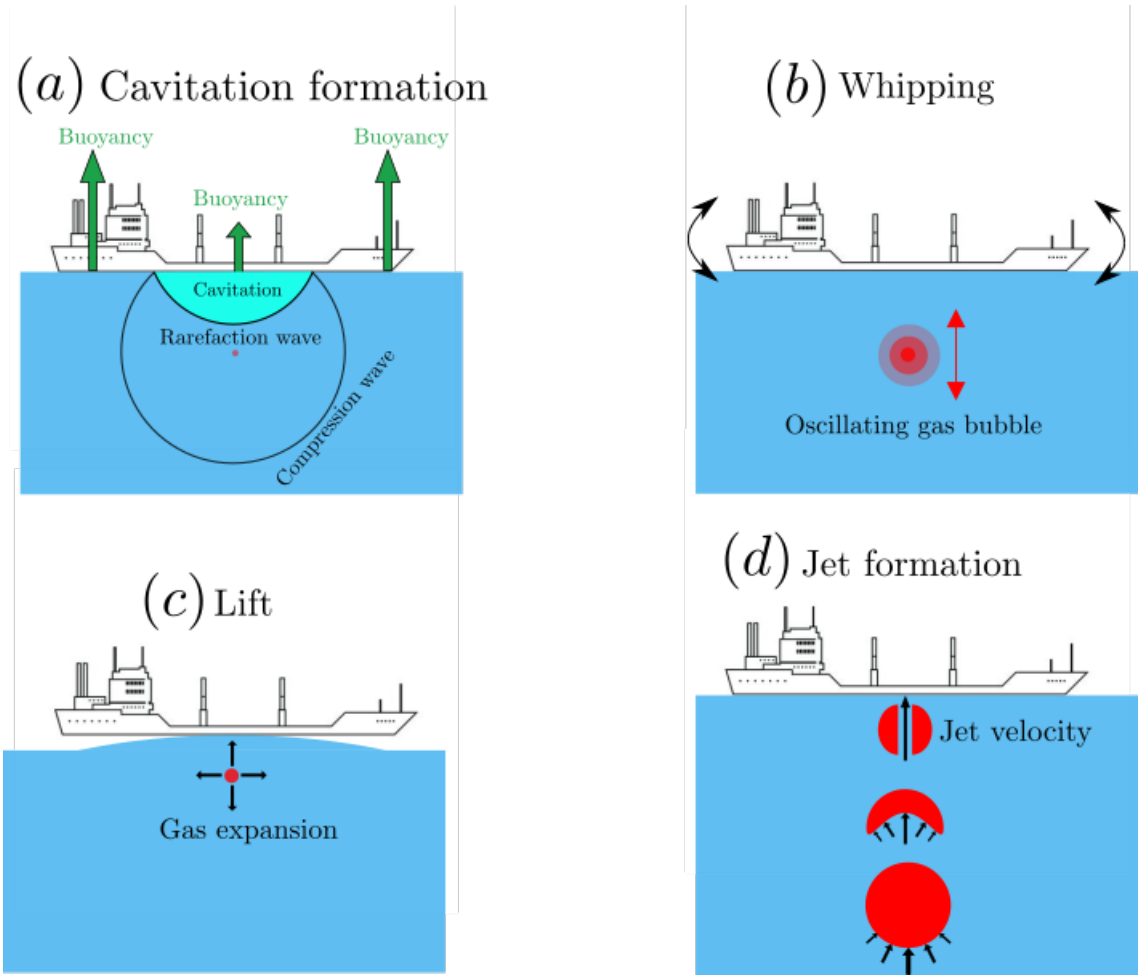

Figure 2.1 An illustration of some of the various damage mechanisms an underwater explosion can cause to a ship. (a) The initial shock wave is reflected as a rarefaction wave at the free surface resulting in a cavitation region of low buyoancy. (b) The bubble oscillation gives rise to an oscillating pressure field, which may excite the normal modes of the ship. (c) As the bubble expands the water surface may deform, which causes stress on the ship. (d) Bubble oscillations sufficiently close to the ship may lead to jet formation. The impact of the jet and ship may cause severe damage.

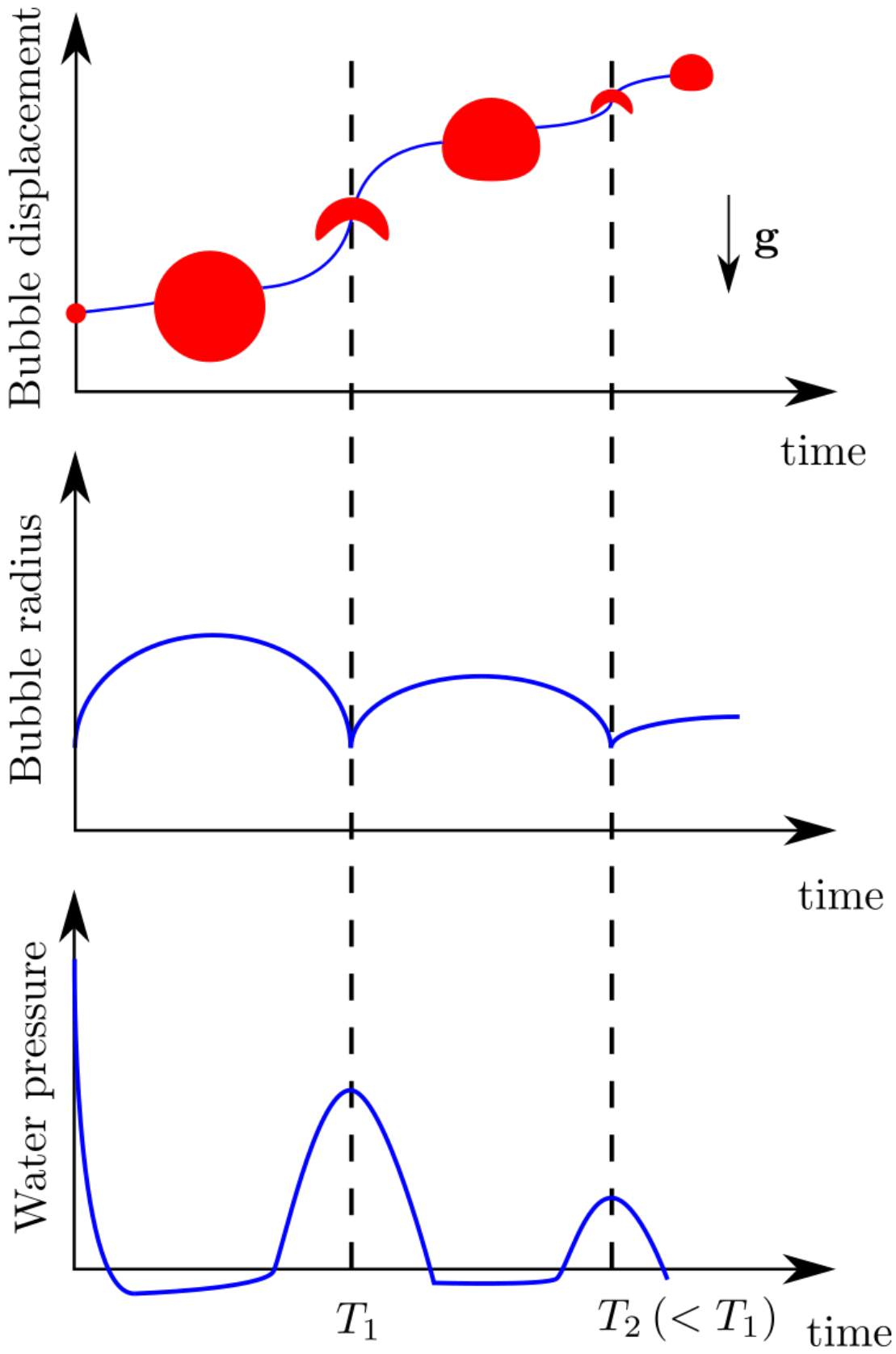

Figure 2.2 *A qualitative description of bubble displacement, bubble radius, and the emitted pressure waves as a function of time. The water pressure is measured at a fixed distance from the bubble. The figure is based on [1].*

3 Empirical relationships

At the time of writing, the most extensive and complete work on underwater explosions is Cole's textbook [2], where several properties discussed in the previous section is derived from first principles. The work on underwater explosions at the Norwegian Defence Research Establishment (FFI) is limited. Detailed analytical work can be found in [3, 4], a concise introduction to some undex phenomena can be found in [5], and an in-house numerical model for underwater explosions have been developed in [6] and [7]. In this section we will summarize the existing empirical relationships and data that are available and well documented for underwater explosions. We emphasize that all of the empirical relationships are based on 70-80 year old data, and therefore should be viewed with a healthy bit of skepticism.

3.1 The similitude equations for the pressure history

The equations of motion and the Rankine-Hugoinot relations governing the bulk fluid and shockwave properties respectively, are invariant under the simultaneous scaling of space and time of the form $(\mathbf{r}, t) \rightarrow (\lambda\mathbf{r}, \lambda t)$, where λ is a scalar. This scale invariance has enabled the formation of the so-called similitude equations of the form

$$\text{Parameter} = K\left(\frac{W^{1/3}}{R}\right)^{\alpha}. \tag{3.1}$$

Here K and α are empirical constants, while W and R are the charge mass and stand-off distance respectively. A derivation of the functional dependence can be found in App. A. In Eq. (3.1) the parameter can be either the peak shockwave pressure p_m, the reduced time constant $\theta/W^{1/3}$, the reduced impulse $I/W^{1/3}$, or the reduced energy flux density $E/W^{1/3}$.

The pressure history at the point of measurement $(\mathbf{r}, t)$ right after the shockwave has passed can be expressed as [8]

$$p(\mathbf{r}, t) = p_m e^{-t/\theta}. \tag{3.2}$$

From Eq. (3.2) the impulse and energy-flux density is defined implicitly through the pressure history as

$$I(\mathbf{r}) = \int_0^{5\theta} p(\mathbf{r}, t)\mathrm{d}t, \quad \text{and,} \quad E = \frac{1}{\rho_0 c_0}\int_0^{5\theta} p^2(\mathbf{r}, t)\mathrm{d}t \tag{3.3}$$

respectively. Here ρ_0 and c_0 refer to the density and speed of sound in the undisturbed water. The upper limit of integration 5θ is chosen by convention. The similitude equations, summarized in Table 3.1, were developed by the Naval Ordnance Laboratories (NOL) in the 1940-1960s. Note that the experimental parameters K and α are very similar for the various types of explosives. In practice, this means that the choice of explosive is not too important for shockwave phenomena as shown in Fig. 3.1.

Table 3.1 The empirical constants in the similitude equations for various explosives. Additional data can be found in [1, 9] and the refereces therein. The original source publication is [10].

Explosive	p_m [MPa]		$\theta/W^{1/3}$ [ms/kg$^{1/3}$]		$I/W^{1/3}$ [kPa s/kg$^{1/3}$]		$E/W^{1/3}$ [m kPa/kg$^{1/3}$]		Range of validity, p_m [MPa]
	K	α	K	α	K	α	K	α	
TNT	52.4	1.13	0.084	-0.23	5.75	0.89	84.4	2.04	3.4-138
Pentolite	56.5	1.14	0.084	-0.23	5.73	0.91	92.0	2.04	3.4-138
H-6	59.2	1.19	0.088	-0.28	6.58	0.91	115.3	2.08	10.3-138
HBX-1	56.7	1.15	0.083	-0.29	6.42	0.85	106.2	2.00	3.4-60
HBX-1	56.1	1.37	0.088	-0.36	6.15	0.95	107.2	2.26	60-500
HBX-3	50.3	1.14	0.091	-0.22	6.33	0.90	90.9	2.02	3.4-60
HBX-3	54.3	1.18	0.091	-0.22	6.70	0.80	114.4	1.97	60-350

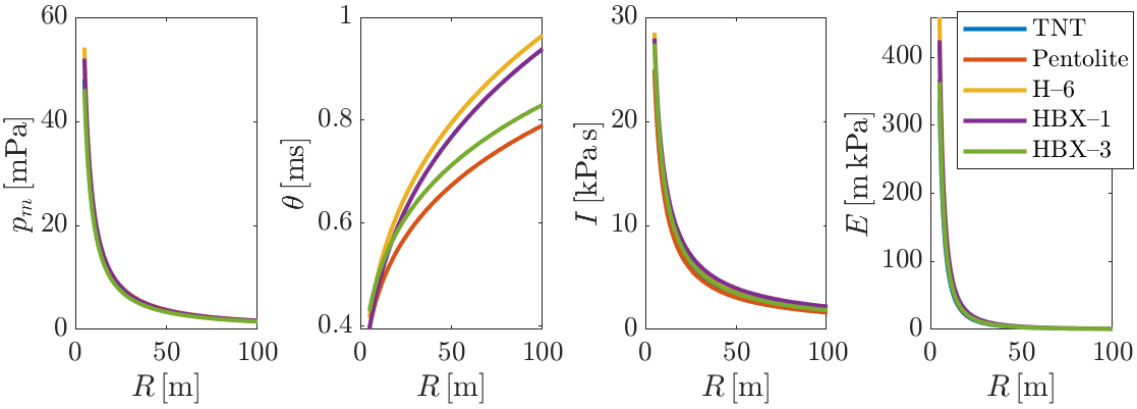

Figure 3.1 The peak pressure p_m, decay constant θ, impulse I, and energy flux density E as a function of stand–off distance R, for a shockwave emitted from various 100 kg *explosive charges.*

After the initial shockwave, the pressure at the point of measurement $(\mathbf{r}, t)$ drops rapidly, to values below the hydrostatic pressure. The phase where the pressure stays below the hydrostatic pressure is called the negative phase. Eventually, when the bubble is at its smallest a new pressure pulse is emitted, resulting in a new, albeit smaller, peak in the pressure history, followed by another rapid decay and subsequent negative phase. These features are sketched in Fig. 3.2. The relevant parameters obey the modified similitude equations

$$\text{Parameter} = K Z_0^{\alpha} \left(\frac{W^{1/3}}{R} \right)^{\beta}, \tag{3.4}$$

where $Z_0 = Z + 10$. Here Z is the initial depth of the explosive in meters[1]. The experimental parameters and constants are given in Table 3.2

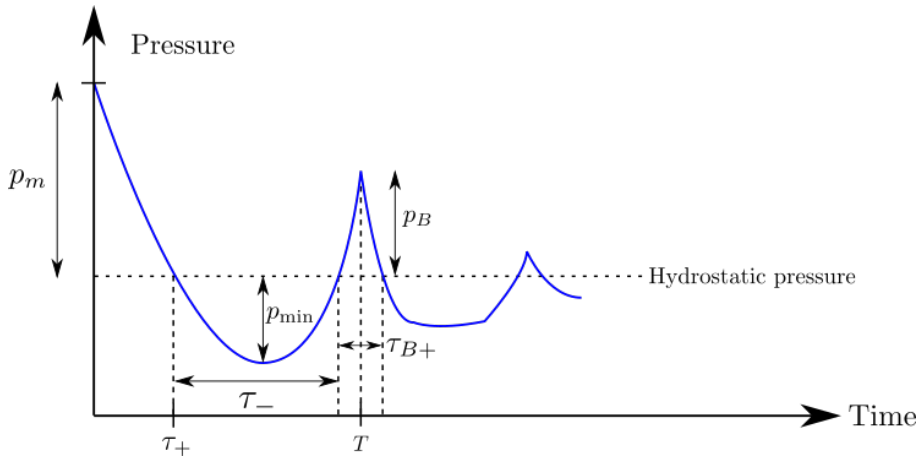

Figure 3.2 A qualitative sketch of the pressure history at a fixed point of measurement.

Table 3.2 The table presents the pressure-history characteristics of deep TNT explosions.

Parameter	Definition	K	α	β	Range of validity
P_m	Max. pres. – 1st positive phase	50.4	0	1.13	$79 < R/W^{1/3} < 5500$
P_B	Max. pres. – 2nd positive phase	9.03	0	1.00	$152 < Z_0 < 1219$
P_B	——— " ———	2.917	1/6	1.00	$1219 < Z_0 < 4572$
$P_{\min}$	Min. pres. - 1st negative phase	-312.94	1/3	1.00	$1372 < Z_0 < 4267$
$P_{\min}$	——— " ———	-28.987	2/3	1.00	$152 < Z_0 < 1372$
$I_+/W^{1/3}$	Imp. – 1st positive phase	36.2	-1/3	0.97	$198 < R/W^{1/3} < 5500$
$I_B/W^{1/3}$	Imp. – 2nd positive phase	86.2	-2/5	1.00	$198 < R/W^{1/3} < 3174$
$E_+/W^{1/3}$	En. flux den. – 1st positive phase	214.9	-1/5	2.07	$198 < R/W^{1/3} < 5500$
$\tau_+/W^{1/3}$	1st positive phase duration	0.368	-5/6	0.00	$152 < Z_0 < 1372$
$\tau_+/W^{1/3}$	——— " ———	0.0117	-2/5	0.00	$1372 < Z_0 < 6708$
$\tau_-/W^{1/3}$	1st negative phase duration	1.499	-5/6	0.00	$198 < Z_0 < 4267$
$\tau_{B+}/W^{1/3}$	2nd positive phase duration	0.532	-5/6	0.00	$198 < Z_0 < 1372$
$\tau_{B+}/W^{1/3}$	——— " ———	0.099	-3/5	0.00	$1372 < Z_0 < 6706$
$T/W^{1/3}$	1st period	2.098	-5/6	0.00	$196 < Z_0 < 4267$

[1] In American units this is often written $Z_0 = Z + 33$, representing the fact that 1 atm weighs the same as 33 feet (10 meters) of sea water. Every 33rd feet (10th meter) down into the water the pressure increases by 1 atm. This observation is informally known as the scuba dive rule.

3.2 Bubble pulsation and the Willis formula

There are also well-established empirical formulas for the first maximum radius R_m and first pulsation period T for free-field underwater explosions,

$$R_m = J\left(\frac{W}{Z+10}\right)^{1/3}, \quad \text{and} \quad T = K\frac{W^{1/3}}{(Z+10)^{5/6}}. \tag{3.5}$$

Here the detonation depth Z is expressed in meters, and J and K are dimensional empirical constants. The exponents are derivable from first principles as shown in App. B. The empirical constants vary from explosive to explosive as shown in Table 3.3. We emphasize that Eq. (3.5) is only valid for the first pulsation, while the subsequent pulsations have smaller radii and shorter periods. In Fig. 3.3 we plot the maximum radius and period for various 100 kg explosive charges as a function of detonation depth.

Table 3.3 The empirical constants for various explosives, based on several experiments after the second world war.

	TNT	Pentolite (PETN + TNT)	HBX-1	HBX-3	H-6
$K\left[\frac{\mathrm{sm}^{5/6}}{\mathrm{kg}^{1/3}}\right]$	2.11	2.11	2.41	2.63	2.62
$J\left[\frac{\mathrm{m}^{4/3}}{\mathrm{kg}^{1/3}}\right]$	3.38	3.52	3.96	4.27	4.09

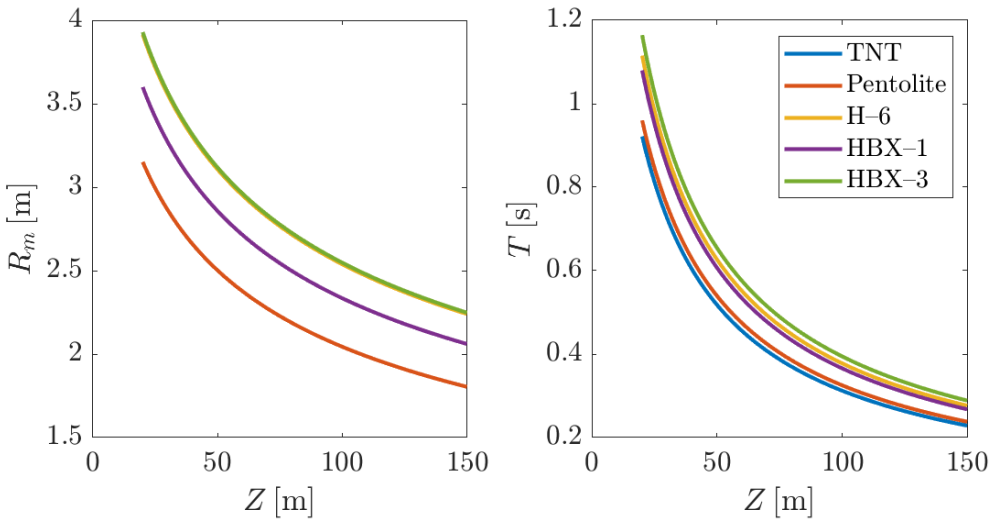

Figure 3.3 The maximum radius and period as a function of detonation depth, during the first oscillation of a bubble resulting from a 100 kg *explosive charge.*

The bubble pulsation is damped, in the sense that the bubbles internal energy decays with time. The primary mechanism causing this damping is compressibility effects of the surrounding water. In particular, the radiation of secondary pressure waves has been identified as a key energy loss

mechanism. Other possible damping mechanisms are irreversible energy transfer to the surrounding water, creation of turbulence, jet formation, and the partly breakup of the bubble surface into spray jets which cool the gas (Taylor instability).

Nevertheless, for subsequent pulsations the equations above should hold if the initial charge weight W is replaced by the residual energy of the nth pulse E_n. In that case, the nth maximal bubble radius, and oscillation period can be expressed as

$$R_{\max,n} = J_1 \left(\frac{E_n}{Z_n + 10} \right)^{1/3}, \quad \text{and,} \quad T_n = K_1 \frac{E_n^{1/3}}{(Z_n + 10)^{5/6}} \tag{3.6}$$

respectively. In the above, we have implicitly assumed that the explosive energy is proportional to the charge weight $E \propto W$ and absorbed the conversion factor into new constants J_1 and K_1. The empirical constants can be eliminated by forming the following recursive relations

$$\frac{R_{\max,n+1}}{R_{\max,n}} = \left(\frac{E_{n+1}}{E_n} \right)^{1/3} \left(\frac{Z_n + 10}{Z_{n+1} + 10} \right)^{1/3}, \quad \text{and} \quad \frac{T_{n+1}}{T_n} = \left(\frac{E_{n+1}}{E_n} \right)^{1/3} \left(\frac{Z_n + 10}{Z_{n+1} + 10} \right)^{5/6}. \tag{3.7}$$

By then inverting Eq. (3.7) we obtain an expression which relates the bubble's energy loss directly to its period, radius, and detonation depth,

$$\frac{E_{n+1}}{E_n} = \left(\frac{R_{\max,n+1}}{R_{\max,n}} \right)^3 \left(\frac{Z_{n+1} + 10}{Z_n + 10} \right) = \left(\frac{T_{n+1}}{T_n} \right)^3 \left(\frac{Z_{n+1} + 10}{Z_n + 10} \right)^{5/2}. \tag{3.8}$$

Equation (3.8) permits an estimate of energy losses in successive contractions from the easily measurable ratio of periods. For deep undex, the ratio of detonation depths can often be set to unity, compared to the ratio of periods, simplifying the expression even further.

Rather surprisingly, there does not seem to be a single well-established empirical expression for the free-field migration Δz of the bubble. Particularly in [2] and [11] two different expressions

$$\Delta z_{\text{Reid}} = 13.2 \frac{W^{11/24}}{(Z + 10)^{5/6}}, \quad \text{and} \quad \Delta z_{\text{Cole}} = 12.2 \frac{W^{1/2}}{Z + 10} \tag{3.9}$$

are given for TNT respectively. In Fig. 3.4 we have plotted the migration as a function of water depth for a 100 kg explosive charge.

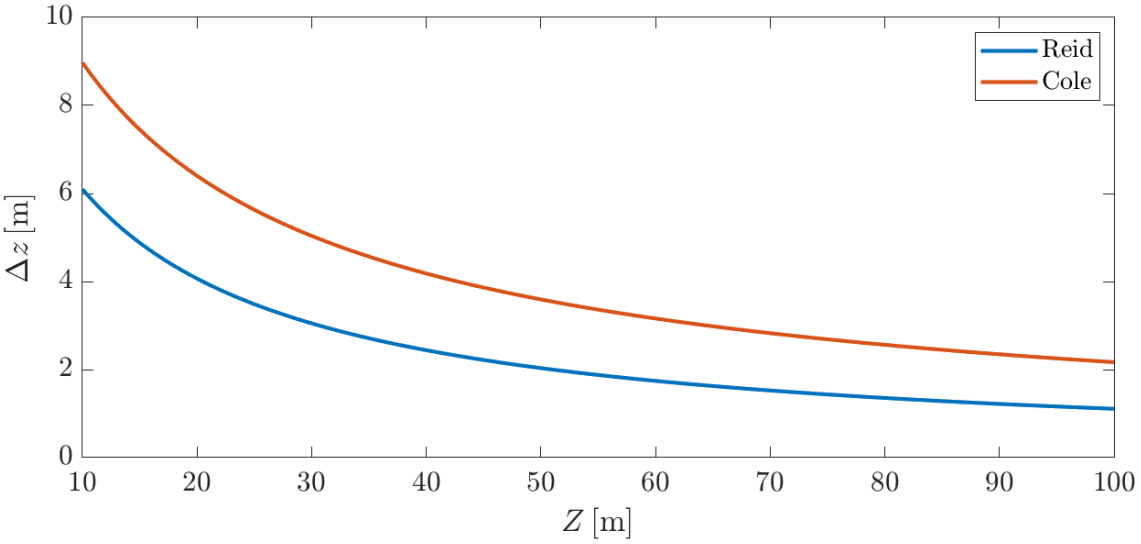

Figure 3.4 The empirical formulas for the migration of a 100 kg *TNT charge as a function of detonation depth.*

3.3 Modern experiments

After the second world war, due to political tension, high–costs, confidentiality, and safety concerns, real–scale undex experiments have become increasingly scarce. Therefore modern undex experiments are usually limited to a much smaller scale. Typically, small explosives (1–10 grams) are detonated in small water tanks (1–10 m^3). The bubble motion and pressure history is recorded with a high–speed camera, and with pressure sensors respectively. In Table 3.4 we provide references to modern papers with experimental data.

There are also modern experiments which generate bubbles via other than explosive means, such as electric sparks and lasers. However, there are fundamental differences between explosion bubbles and spark/laser bubbles. The most obvious difference is that the explosion bubbles are typically larger, and therefore buoyancy plays a more important part in the evolution of the bubble shape. Furthermore, the contents of an explosive bubble contains the detonation products, originating from the explosive, which usually are unable to dissolve in water. On the other hand, the contents of a spark or laser bubble is usually steam which may dissolve as the bubble oscillates. Furthermore, the initial shock wave and subsequent pressure waves originating from an explosion bubble is usually much stronger than those generated by a laser or spark. The larger pressures associated with an explosion can cause changes in the bubble characteristics, either by reflections from the tank walls affecting the pressure in the water or by affecting nearby structures that interact with the bubble. Therefore, for the purposes of mimicking the bubble dynamics of a large scale underwater explosion, small–charge underwater explosions remain the only alternative. We emphasize that the formulas and calculations presented in this report are limited to explosion bubbles only.

Table 3.4 A collection of modern experimental works on small–scale underwater explosions, relevant to our benchmarking purposes.

Year	Reference	Explosive charge	Charge weights	Data	Boundary condition	Comment
2005	Klaseboer et. al. [12]	Hexocire	10 g, 35 g, 55 g	Bubble dynamics Pressure history Elastic deformation	Free–field Rigid Resilient	Clear data by utilization of absorbing walls
2008	Brett et al. [13]	PE-4	5.0 g	Strain load	Horizontal cylinder	Primary focus on strain loading
2010	Hung et al. [14]	Unspecified	1.12 g (TNT)	Bubble dynamics Pressure history Strain load	Free–field Free surface Rigid	Pressure history disturbed by reflections
2013	Zhang et al. [15]	PETN	1.2-9.0 g	Bubble dynamics Pressure history	Free–field Free surface Rigid	Primary focus on numerical method
2016	Cui el al. [16]	PETN	4.0 g	Bubble dynamics Pressure history	Free–field Free surface Rigid surface Free and rigid Rigid with hole Resilient	Unprocessed photographic data of bubble dynamics
2019	Li et al. [17]	PETN	2.5 g	Bubble dynamics Pressure history	Free–field Two–bubble interaction	Primary focus on two–bubble interaction (Related to Cui 2016)
2021	Wang et al. [18]	PETN RDX CL-20	1.0 g	Bubble dynamics Pressure history	Free–field	Focus on comparing the explosives. (Observed the most oscillation periods on this list)

4 Overview of theoretical approaches to free–field bubble dynamics

Accurately modeling the dynamics of a gas bubble formed by an undex is a complicated, as of yet, unresolved issue in modern physics. In this chapter we will briefly summarize some of the important milestones that has been reached at the time of writing. Historically, it is natural to consider three phases:

(I) In the initial approaches, the gas bubble was assumed to remain spherical with zero migration, and was completely decoupled from the shockwave phase. This allowed the bubble motion to be described by relatively simple non–linear differential equations (ODEs). The research culminated in an analytical derivation of the Lamb–Rayleigh–Plesset equation, whose solution describes a pulsating bubble without any energy loss. In practice, this means that the solution describes the first oscillation of the bubble well, but fail to model subsequent oscillations where the bubble motion becomes damped, due to energy loss.

(II) In the intermediate approaches, the goal was to identify the dominant energy loss mechanism(s) in the bubble motion. Several additional effects was included to the Lamb–Rayleigh–Plesset equation through perturbation theory. Concretely, the perturbative analysis included effects such as compressibility, viscosity, migration due to gravity, and small deviations from spherical bubble shape. Of these, the dominant energy loss mechanism is considered to be the compressibility of water.

(III) In modern approaches, we have moved away from the semi–analytical approaches of phase I and II. Instead we focus on solving the Navier–Stokes equations[2] numerically with as few assumptions as possible. For example, it is no longer necessary to assume spherical symmetry of the gas bubble, allowing for the description of jet formation. The field of such numerical approaches, are referred to as computational fluid dynamics (CFD). There are several different numerical methods that can be used, including the finite element method (FEM), the finite volume method (FVM), the boundary integral method (BIM), and smoothed–particle hydrodynamics (SPH).

For completeness, we will in the next three sections briefly discuss some concrete aspects of the aforementioned phases. However, we will wherever possible avoid complicated mathematical derivations to keep this report to a modest length. Instead we will refer to either the references or the appendix that hopefully provides sufficient mathematical detail.

4.1 Phase I: The Lamb–Rayleigh–Plesset equation

Due to its historical importance, mathematical simplicity, and because it provides physical insight even in today's more modern approaches we will in the following introduce the equation of motion that was initially utilized to describe bubble dynamics. A detailed derivation can be found in App. C.1.

The equation of motion governing the bubble oscillation follows directly from the conservation

[2]The Navier–Stokes equations are the governing equations of motion for fluid dynamics. They are incredibly difficult to solve, despite their wide range of practical use. As of yet it has not been proven whether or not smooth solutions always exists in three dimensions. This is called the Navier–Stokes existence and smoothness problem. It is recognized as one of the most important open problems in mathematics, earning it a place among the seven millenium problems for which the Clay Mathematics Institute offer $1 million USD for a proof or counterexample.

of mass, momentum, and force balance at the bubble–liquid interface. The necessary assumptions are that the bubble retains spherical symmetry, is surrounded by an incompressible fluid, and that the thermodynamics inside the bubble is uniform. The equation of motion then takes the form

$$\frac{2\gamma}{R\rho} + R\ddot{R} + \frac{3}{2}\dot{R}^2 + 4\frac{\nu}{R}\dot{R} = \frac{p_b - p_\infty}{\rho} \quad \text{where,} \tag{4.1}$$

- The equation is solved for $R(t)$, the time–dependent bubble radius.
- The constants ρ and ν are the density and kinematic viscosity of the liquid respectively.
- The constant γ is the surface tension at the bubble–liquid interface.
- The time dependent driving term $p_b - p_\infty$, is the pressure difference between the bubble and external liquid far away from the bubble.

Equation (4.1) is widely known as the Rayleigh–Plesset equation, due to Rayleigh's work on imploding cavities [19] and Plessets work on bubble dynamics [20]. Nevertheless, the first actual appearance of the equation in a scientific paper was made by Lamb in 1923 [21]. We shall avoid misattribution and refer to it as the Lamb–Rayleigh–Plesset equation.

Note that the Lamb–Rayleigh–Plesset equation is not restricted to gas bubbles formed by undex[3]. The equation can be used to determine the bubble radius as a function of time $R(t)$, for in principle any gas bubble satisfying the underlying assumptions. The dynamics of the bubble is governed by its pressure difference with its surroundings. In general, the external pressure p_∞ can either be a constant or be a time–dependent function thus acting as a driving term. For the undex it is customary to choose $p_\infty = p_{\text{atm}} + \rho g z$ as the hydrostatic pressure at the depth of detonation z. The bubble pressure $p_b(t)$ is given by the physical processes occurring inside the bubble. From a physical point of view it has been customary to consider the pressure inside the bubble to consist of two terms

$$p_b(t) = p_v + C/V_B^\gamma(t). \tag{4.2}$$

Here p_v represents the pressure for vapour–liquid equilibrium such that no gas escapes from the bubble. The second term requires the gas to obey an adiabatic[4] gas law, where γ is the adiabatic gas constant (also known as the heat capacity ratio). The time–dependent bubble volume is taken to be $V_B(t) = \frac{4\pi}{3}R^3(t)$. More complex constituent relations, such as the Jones–Wilkins–Lee equation of state for explosives [22], are of course possible.

Being non–linear the Lamb–Rayleigh–Plesset equation is by no means trivial to solve analytically. A discussion of its several properties and applications other than undex can be found in [23]. To illustrate the solutions relevant to undex we have solved Eq. (4.1) numerically, with the constituent

[3] In the static case (R = const) the Rayleigh–Plesset equation simplifies to the Young–Laplace equation

$$p_b - p_\infty = \frac{2\gamma}{R}.$$

Its physical interpretation is that even though the pressure inside the bubble is larger than the external pressure the bubble does not expand because the outward force is exactly balanced by the surface tension.

[4] More accurately, the process is polytropic. A polytropic process is a thermodynamic process that obeys the relation $pV^K = C$. If $K = 1$ the process is isothermal and if $K = \gamma = C_P/C_V$ the process is adiabatic. For gases arising from explosions γ is usually replaced by an appropriate K. The value of K lies somewhere between 1 (isothermal ideal gas) and 1.4 (diatomic ideal gas/air).

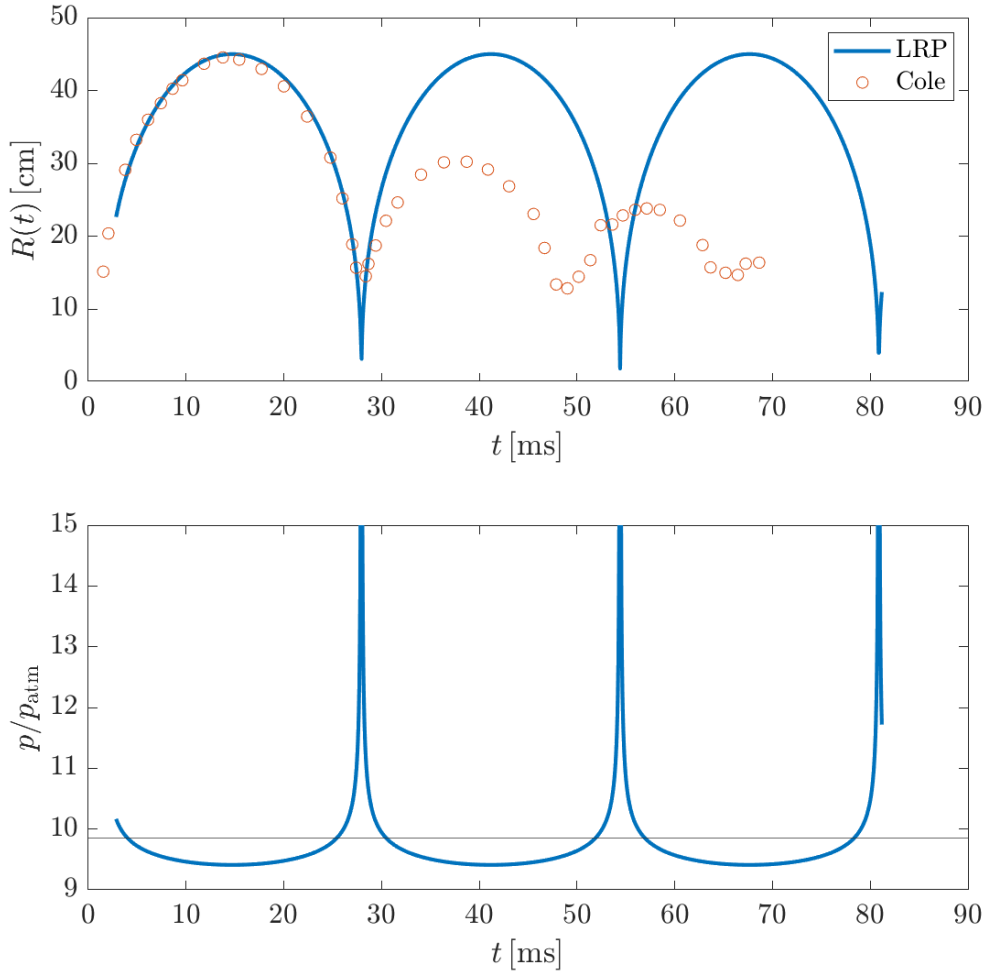

Figure 4.1 *The experimental data (Cole) and numerical solution of the Lamb–Rayleigh–Plesset (LRP) equation for a 0.25 kg tetryl charge detonated 91.44 m below the water surface. The pressure is normalized with respect to the atmospheric pressure p_{atm}. The horizontal line corresponds to $p_\infty = p_{\text{atm}} + \rho g z$.*

relation in Eq. (4.2). The technical details of the numerical solution can be found in App. C.2. To asses the validity of the Lamb–Rayleigh–Plesset equation we will compare the radius–time curve with an empirical one given on p. 271, Fig. 8.1 in Cole's book [2]. The case is a 0.25 kg tetryl charge detonated 91.44 m below the water surface.

The numerical solution and experimental data is plotted in Fig. 4.1. Note that despite its simplicity, the numerical solution captures many of the qualitative features relevant for undex. The period, maximum radius, and general behaviour fits nicely with the experimental values for the first oscillation. For subsequent oscillations, the theory deviates from the experiment. The most serious qualitative issue is that the damping in the numerical solution occurs on a surrealistically long time scale. This is interesting given that both viscosity and surface tension is present in the surrounding

water, and indicates that neither viscosity nor surface tension are the causes of damping of the radial motion for large bubbles.

Finally, we comment on the pressure distribution in the surrounding liquid. In terms of the bubble volume $V_B(t) = 4/3\pi R^3(t)$ the pressure distribution at a point $(\mathbf{r}, t)$ outside of the bubble can be expressed as

$$p(\mathbf{r}, t) = p_\infty + \rho \left[\frac{\ddot{V}_B(t)}{4\pi|\mathbf{r}|} - \frac{\dot{V}_B^2(t)}{32\pi^2|\mathbf{r}|^4} \right]. \tag{4.3}$$

In Fig. 4.1 we have, for illustrative purposes, plotted the pressure history in Eq. (4.3) at the fixed point $|\mathbf{r}| = 10\,\text{m}$. The volume acceleration term dominates near the minimum of the bubble, and it accounts for the pressure in the primary shock wave and the subsequent pressure peaks. The volume velocity term is known as the "afterflow" pressure. The afterflow dominates between pressure peaks, but is suppressed at large distances from the bubble.

Note that there is an instantaneous response between the bubble motion and the emitted pressure waves a finite distance away from the bubble. This is evident in Eq. (4.3) as both the response (left hand side) and disturbance (right hand side) occurs at the same time t. This is a consequence of that we have assumed the liquid to be incompressible such that the speed of sound is infinite.

4.2 Phase II: Perturbative corrections

The most significant assumptions of the Lamb–Rayleigh–Plesset equation is that compressibility, gravity, and deviations from spherical form are neglected. The Lamb–Rayleigh–Plesset equation was the inspiration for several subsequent publications attempting to add various complexities to the equation, through appropriate perturbations. Several of the most important perturbations are discussed in Cole's book [2], but there are also significant works after this. Due to the large number of publications we will here attempt to discuss the result of the most important perturbations only qualitatively.

4.2.1 Effects of gravity

As mentioned previously gravity leads to a buoyancy force pushing the bubble upwards, and a deviation from spherical shape. By assuming the correction for gravity to be small, the velocity potential, pressure, and bubble radius vector can be expanded in powers of the acceleration of gravity g. Since, the unperturbed state exhibits spherical symmetry, the spherical harmonics are used as basis functions in the expansion. The first order correction to the bubble radius vector simply becomes an equal upward displacement for all points on the bubble surface, without any distortion of the spherical shape. The velocity of each point on the bubble surface during the uniform upward displacement is given by the Herring migration formula

$$U = \frac{2g}{R^3} \int_0^t R^3 \mathrm{d}t. \tag{4.4}$$

Note that the velocity increases with time, and attains its maximum value when the bubble is at its smallest due to the term $1/R^3$. Hence, consistent with our discussion in the introduction, the bubble migrates the most during the contraction phase and the least when the bubble is relatively large. A similar kind of perturbative analysis reveals that the shape of the bubble deviates the most from a sphere during its contraction phase.

4.2.2 Effects of compressibility

One of the most serious issues, with the Lamb–Rayleigh–Plesset equation is the lack of damping, despite the inclusion of viscosity, as illustrated in Fig. 4.1. The discussion of bubble motion so far has been based on the assumption that the surrounding water is incompressible. Energy conservation dictates that in this scenario the explosive energy left after emission of the shock wave is assumed to be distributed entirely into potential and kinetic energy of the water flow plus the internal energy of the gas. In this approximation, the undamped solution for the bubble radius indicates that there is no substantial mechanism of energy loss, so that the total energy is reversibly transferred back and forth between the gas bubble and the surrounding water. The energy losses actually occurring during the motion cannot be described without taking into account new mechanisms by which energy can be dissipated.

The primary mechanism responsible for the energy loss turns out to be the compressibility of water. As the bubble expands the water particles close to the bubble interface are squished together, forming a local region of high density known as a compression wave. Unlike the bulk of the fluid, the compression wave never reverses its velocity, but travels to infinity continously loosing energy through heat dissipation. Energy is therefore lost from the system, because the gas bubble performed work to create the compression wave. Each bubble cycle produces one compression wave, leading to a gradual loss of bubble energy with each subsequent pulsation. The principle is illustrated in Fig. 4.2. In other areas of fluid mechanics, this effect is known as the acoustic radiation[5] of sound since the compressed wave propagates at the speed of sound.

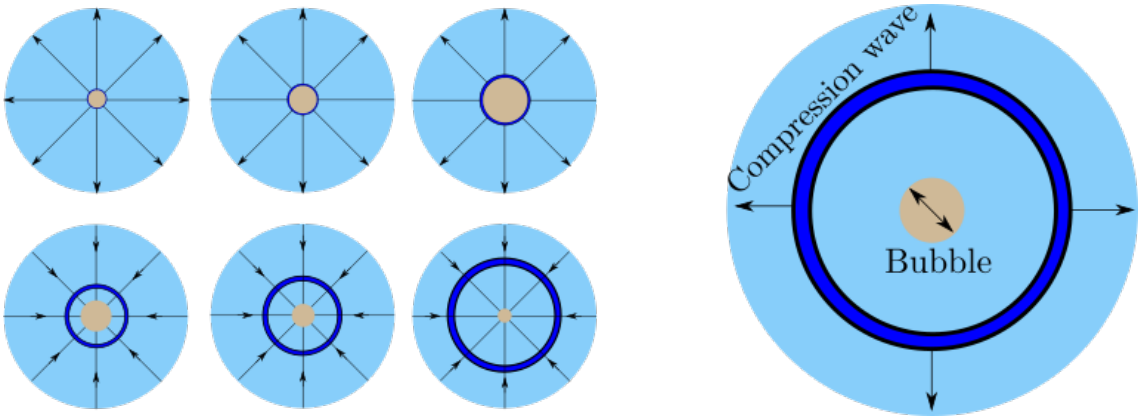

Figure 4.2 The formation of compression waves by the bubble expansion due to finite water compressibility. In an incompressible fluid, there would not be a build up of particles close to the bubble interface.

In technical terms, incorporating a compressible fluid modifies the conservation of mass

$$\text{from} \quad \nabla \cdot \mathbf{v} = 0 \quad \text{to} \quad \nabla \cdot \mathbf{v} = -\left(\frac{1}{\rho}\frac{\mathrm{d}\rho}{\mathrm{d}t}\right) = -\left(\frac{1}{c^2\rho}\frac{\mathrm{d}p}{\mathrm{d}t}\right) \neq 0. \tag{4.5}$$

Here $c^2 = (\mathrm{d}p/\mathrm{d}\rho)_S$ is the surrounding liquids speed of sound, and we must find an appropriate equation of state relating the pressure and density of the liquid.

[5]The use of the word radiation most likely stems from electromagnetic theory, where an accelerating electric charge produces pulses of EM waves, travelling at the speed of light, which we call radiation.

A direct consequence of the inclusion of a finite speed of sound, is the introduction of a finite response time. In a compressible model, a disturbance (in the origin) emitted at time t propagates with a constant velocity c and reaches a point $r > 0$ in a time r/c. Consequently, there is a delayed response time $t - r/c$ between cause and effect, which we call the retarded time. This effect is perhaps the most visible in the expression for the pressure field in the surrounding liquid

$$p(\mathbf{r}, t) = p_\infty + \rho \left[\frac{\ddot{V}_B(t - r/c)}{4\pi|\mathbf{r}|} - \frac{\dot{V}_B^2(t - r/c)}{32\pi^2|\mathbf{r}|^4} \right] + \dots, \tag{4.6}$$

where the dots $(\dots)$ denote higher order terms that vary depending on the specific formulation (e.g. equation of state) of the model. Importantly, note that although Eqs. (4.6) and (4.3) formally look very similar, the time dependence of $V_B(t)$ is fundamentally different due to the presence of damping.

A concrete example for a model describing the oscillation of a bubble in a compressible liquid is the Keller–Kolodner equation [24, 25] of the form

$$R\ddot{R}\left(1 - \frac{\dot{R}}{c}\right) + \frac{3}{2}\dot{R}^2\left(1 - \frac{\dot{R}}{3c}\right) = \frac{p_b - p_\infty}{\rho}\left(1 - \frac{\dot{R}}{c}\right) + \frac{R}{\rho c}\dot{p}_b. \tag{4.7}$$

Note that in the limit $c \to \infty$, corresponding to an incompressible fluid, the Keller–Kolodner equation reduces to the Lamb–Rayleigh–Plesset equation. Physically, it is natural that higher order terms in the Lamb–Rayleigh–Plesset equation should be proportional to factors of $1/c$, because in undisturbed water the speed of sound (1480 m/s) is relatively high. The term proportional to $\dot{p}_b$ is the most important, as it physically represents the acoustic radiation of energy. In Fig. 4.3 we present the numerical solution of Eq. (4.7) and compare with the previously discussed experiment, as well as the corresponding solution of the Lamb–Rayleigh–Plesset equation. We observe that including compressibility significantly improves the correlation between theory and experiment. This supports the current consensus, which is that the compressible nature of the liquid accounts for the most significant portion of the energy loss during the bubble pulsation.

However, as we see from Fig. 4.3, there is still deviation between theory and experiment for subsequent oscillations even when incorporating compressibility. Most likely, the explanation is that there are additional energy loss mechanisms than just compressibility. Examples of possible energy loss mechanisms are turbulence, heat transfer, and jet formation. The jet formation is a particularly promising candidate because it is the most dramatic event that occurs close to the end of the bubble motion. Thus it is reasonable to expect that it should account for a large energy loss during the final pulsations of the bubble. Furthermore, none of the semi–analytical approaches discussed in this section are able to incorporate it because the relevant perturbation theory breaks down during strong deviations from spherical symmetry.

There are several other semi–analytical models incorporating bubble dynamics of varying degrees of complexity in addition to the Keller–Kolodner equation. In Tab. 4.1. we provide a list of alternative formulations and briefly comment on some of their differences. A particularly interesting point, is that bubble models describing both dilational and translational modes typically treat the surrounding water as incompressible. We speculate that the reason for this is that the mathematics quickly becomes rather unwieldy if both effects are included simultaneously, despite the number of simplifying assumptions being made. This unavoidable mathematical complexity suggests that pure numerical simulations are the way of the future. In App. D we provide a concise mathematical overview of some of the most important semi–analytical models.

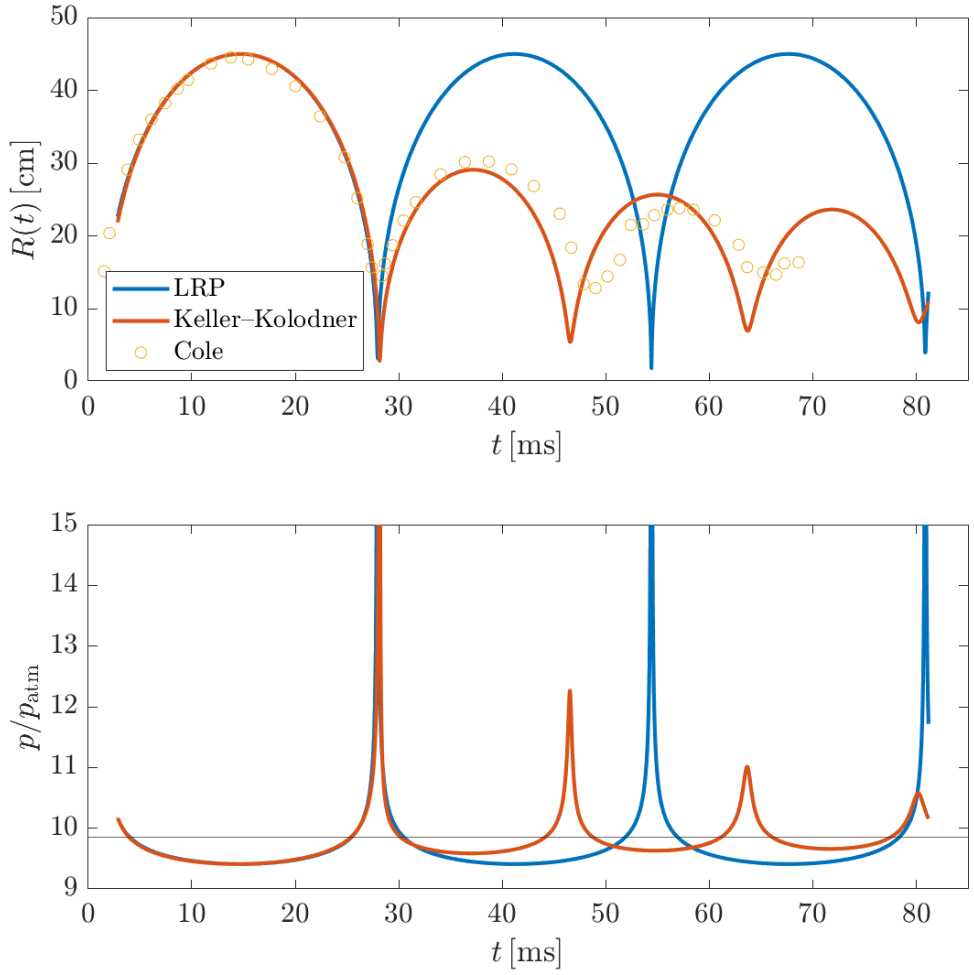

Figure 4.3 The numerical solution of both the Lamb–Rayleigh–Plesset (incompressible) and Keller–Kolodner (compressible) equation, compared with the experimental data for a 0.25 kg tetryl charge detonated 91.44 m below the water surface.

Table 4.1 A brief collection of historically important publications associated with the development of bubble dynamics. Due to the large amount of publications the list can not be considered complete.

Year	Reference	Compressible	EOS for water	Dilation	Translation	Historical relevance
1923	Lamb–Rayleigh–Plesset [19, 20, 21]	No	None	Yes	No	Starting point with zero perturbations
1941	Herring [26]	Yes	Linear	Yes	No	Introduction of compressibility
1941	Herring [26]	No	None	Yes	Yes	Introduction of migration
1943	Taylor [27]	No	None	Yes	Yes	Improvement of migration
1952	Gilmore [28]	Yes	Nonlinear	Yes	No	Introduction of Tait equation for water
1953	Keller–Kolodner [24, 25]	Yes	Linear	Yes	No	Systematization of bubble motion (book series)
1953	Keller–Kolodner [29]	No	None	Yes	Yes	Systematization of bubble motion (book series)
1986	Prosperetti–Lezzi [30, 31]	Yes	Nonlinear	Yes	No	Generalization of bubble dilation models
2002	Geers–Hunter [32]	Yes	Linear	Yes	Yes	Coupling between shockwave and bubble Introduction of gas–liquid impedance

4.3 The Kelvin impulse and bubble–surface interaction

So far we have only looked at a free–field underwater explosion in an infinite medium, without any nearby structures. However, of special interest is to determine exactly what happens when the bubble interacts with a structure, say for instance a ship or submarine. In this section we will provide a general overview of the simplest possible bubble–surface interactions. We refer the reader to App. E where we provide the mathematical details.

If a gas bubble pulsates in the vicinity of a rigid (free) surface, the bubble will tend to be attracted (repelled) by the surface. If the bubble is close to the surface jet formation may also occur. Most of the migration, either towards or away from the surface, occurs when the bubble is at its smallest. The force causing this apparent attraction or repulsion is known as the Bjerknes force, and it is a geometrical consequence of the surface breaking translational symmetries. The direction of the bubble migration coincides with the direction of the bubble's so-called Kelvin impulse [33, 34, 35] at the time the bubble is at its smallest.

The direction of the bubble migration is determined by a competition between two forces. The buoyancy force attempts to lift the bubble towards the water surface, and the Bjerknes force tries to attract (repel) the bubble towards a rigid (free) surface. The Bjerknes force is stronger, the closer the bubble is to the relevant surface. Therefore, there exists a critical distance between the bubble and surface where the Bjerknes force dominates the buyoancy force. For a bubble a distance ξ from either a rigid or free surface with maximum radius $R_{\max}$ we introduce the dimensionless distance $\gamma = \xi/R_{\max}$. The buyoancy force is parameterized by the so–called buyoancy parameter which approximately is given by

$$\delta = \sqrt{\frac{\rho g R_{\max}}{\Delta p}} \approx \sqrt{\frac{R_{\max}}{Z}} < 1. \tag{4.8}$$

Here ρ is the density of water, g is the gravitational acceleration, Δp is the pressure difference driving the bubble dynamics, and Z is the depth of the explosion. The approximation holds when we neglect the interior pressure of the gas[6].

The simplest possible geometries are eloquently discussed in [36, 37] and are:

1. The bubble oscillating a distance γ above the seabed (or any other plane rigid surface).
2. The bubble oscillating a distance γ directly below the water surface (or any other plane free surface).

For the aforementioned geometries, a detailed mathematical theory, outlined in App. E, reveals that the line

$$\gamma\delta \approx 0.442 \tag{4.9}$$

separates the regions where the buoyancy force and Bjerknes force dominates. Figure 4.4 illustrates the attraction to a rigid surface (a) or the repulsion from a free surface (b) for these simple geometries, and serves as a concrete benchmark for development in Impetus. In the analytical derivation of, Eq. (4.9) there are a few assumptions which makes the expression only an approximation. First, it is assumed that the bubble retains its spherical form for the entirety of the pulsation, which is not true during the collapse phase. Second, the migration distance is considered to be small so the expression is not expected to be valid very close to the rigid surface. Third, the time dependence is governed by the Lamb–Rayleigh–Plesset equation, so the expression is only valid for the first

[6]This is actually more of a convencience than an actual mathematical approximation, since we do not want the buyoancy parameter to be time–dependent.

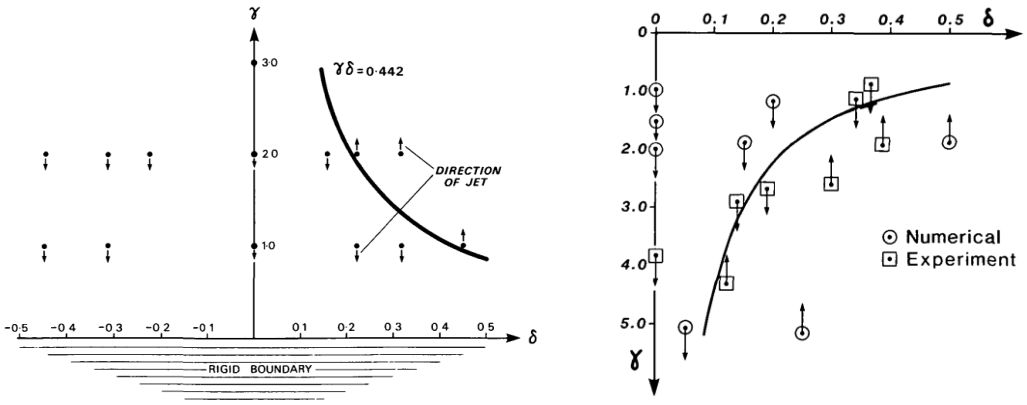

(a) Rigid surface below the bubble. *(b) Free surface above the bubble.*

Figure 4.4 The partitioning of the (γ, δ) phase space for (a) a rigid boundary and (b) a free surface. The apparent repulsion or attraction to the surface originates from a competition between the Bjerknes and buoyancy force. The arrows indicate the direction of migration or jet. Figure taken from [35].

pulsation. In practice, this means that the partitioning of the (γ, δ) phase space is not exact close to the critical line, but the numerical simulations and experiments in 4.4 indicates that it is a good approximation to describe the first pulsation.

In subsequent publications [38, 39], Eq. (4.9) has been improved by lifting certain assumptions. The authors generalize to a wider class of possible surfaces, specifically to rigid surfaces of revolution, two-fluid interfaces, inertial and membrane boundaries.

For benchmarking purposes it is more than sufficient to consider the bubble's Kelvin impulse for a geometry where the rigid surface is inclined by an angle β with respect to the horizontal, as shown in Fig. 4.5. In such a geometry, the Bjerknes force attempts to pull the bubble towards the rigid surface and the buoyancy force tries to lift the bubble upwards. The Kelvin impulse therefore takes the form

$$\mathbf{I}_{\text{Bubble}} = I_{\text{Bjerknes}}\boldsymbol{\Gamma} + I_{\text{Buyoancy}}\mathbf{k}. \tag{4.10}$$

Equation (4.10), in its full glory, is given in the App. E as Eq. (E.10). The direction of the Bjerknes force is parallel to the normal vector (pointing away from the bubble) of the rigid surface, and is given by

$$\boldsymbol{\Gamma} = \frac{1}{\gamma^2}\left(\mathbf{i}\sin\beta - \mathbf{k}\cos\beta\right). \tag{4.11}$$

The usefulness of Eq. (E.10) is that it can be used to determine the direction of migration for different orientations of the rigid surface, which will be useful in our benchmarking. A concrete example would be to investigate the direction of the bubble migration as a function of the inclination angle of the rigid surface.

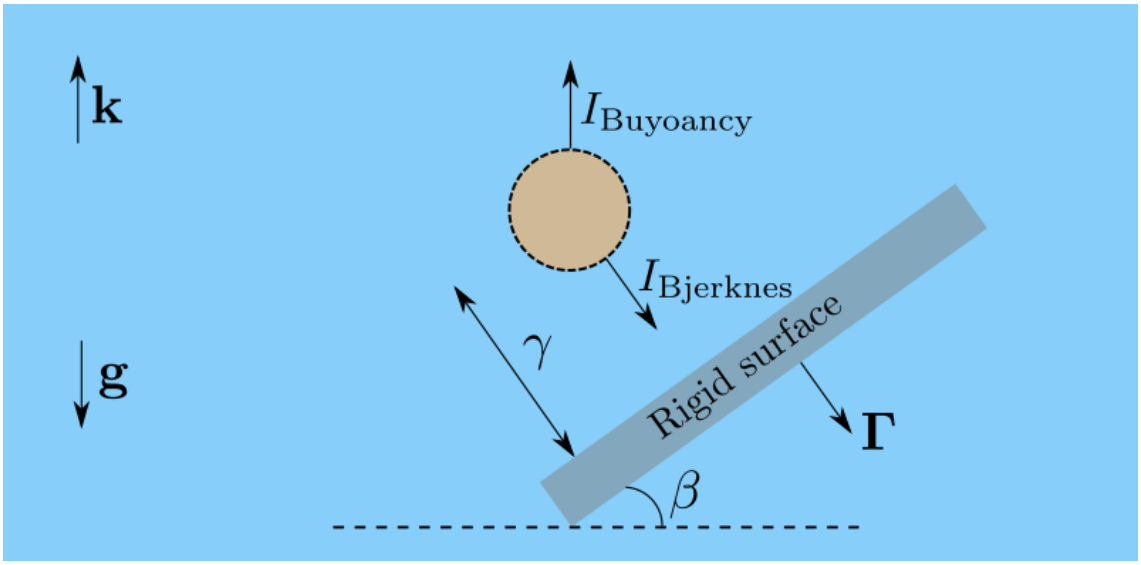

Figure 4.5 The direction of the bubble's Kelvin impulse in the presence of an inclined rigid surface.

4.4 Phase III: Computational fluid dynamics

While the semi–analytical models can reproduce many undex features, full numerical solutions should, in principle, be able to model an undex in full detail.

In general, a numerical solution typically dictates that the domain is discretized into nodes which obeys the equations of motion locally. The characteristics of the nodes are then updated according to the equation of motion in small time steps. The nodes are coupled to each other through various interpolation schemes. Depending on the details of the equations of motion there are several numerical methods that may be suitable. In broad strokes the methods can be divided into mesh–based, particle–based, or a hybrid between the two. Well known examples are the finite element method, finite volume method, Lattice Boltzmann method, and smoothed particle hydrodynamics.

In the context of undex, the most frequently used numerical method is the so–called boundary integral method. The popularity of the method stems from its history as well as numerical efficiency. Historically, it was the first numerical method that was able to describe the bubble pulsation in a satisfactory manner. The jet formation can also be described to a certain extent, but it requires a brute force additional technical step known as the ”surgical cut”. Furthermore, the boundary integral method is limited by the fact that the assumptions of potential flow theory must be satisfied. Concretely, this means that it is impossible to describe real bubble–structure interactions. In App. F we include a simplified and succinct overview of the method. For a more in–depth analysis see the thesis by Best [37].

The restrictions on the boundary integral method has led to a surge in the investigation of developing a good numerical procedure for describing undex. In Tab. 4.2 we provide a list of papers where different numerical methods are used to simulate undex phenomena. As we can see there are a large number of possible choices, each with their own advantages and disadvantages. Typically, the shockwave and bubble dynamics are modeled as separate phenomena because they occur on vastly different timescales. In addition, various numerical methods are usually coupled to

each other to bring out the best of each method. Typical aspects that necessitates such a coupling is that separate methods are used to describe the detonation process, shock propagation, bubble dynamics, and structure deformation.

Table 4.2 A collection of articles employing different numerical methods to simulate undex phenomena. We provide general comments to try and highlight the usefulness of each method. Note that due to the large number of existing articles the list can not be considered complete. Hopefully the included references will provide sufficient technical information to the interested reader.

Numerical method	References	General notes
Boundary integral	[37, 40, 41, 42]	2D mesh discretization Historically the first and most frequently employed method Computationally effective due to dimensional reduction Must be supplemented/modified to describe structure interactions
Finite element	[43]	3D mesh discretization Useful to describe structure deformation
SPH	[44, 45]	Particle discretization Suitable to describe large deformations
Boundary integral + Finite element	[12, 46, 47]	i) Boundary integral, models bubble dynamics ii) Finite element, models structure deformation
LS–Dyna + Boundary integral	[48]	i) LS–Dyna, models detonation process ii) Boundary integral, models bubble dynamics
Boundary integral + SPH	[49]	i) SPH, models detonation process ii) Boundary integral, models bubble pulsation iii) SPH, models jet formation
Boundary integral + SPH shells	[50]	i) Boundary integral, models flow field ii) SPH, models structure deformation
Finite volume method + Volume of fluid	[17, 51]	i) Finite volume, models water domain ii) Volume of fluid, models water–gas interface
Finite element + Volume of fluid	[52]	i) Finite element, models water domain ii) Volume of fluid, models water–gas interface

5 Modeling in Impetus

Having seen the limitations of the analytical modeling of undex, we will attempt to perform full numerical simulations. However, there are several potential pitfalls in pursuing such an endeavour. For our purposes, some of these pitfalls may stem from that Impetus has not been developed with undex applications in mind. Actually, to the best of our knowledge, this is the first time that Impetus is used to model undex phenomena.

Before attempting to model a complex problem, it is very important that the numerical code first is validated against simpler problems for which the answer is known. This presents another challenge since, as we have seen, quite a lot of the experimental undex data is old and contains large uncertainties, whereas the available analytical models are too simplified to approximate the real problem. It is therefore not obvious how to determine whether discrepancies between numerical simulation and empirical/analytical formulas is due to errors in the numerical approach or uncertainties in the experimental data. Still, we know at least some features, given in Tab. 5.1, of an undex process that a numerical simulation should be able to reproduce.

Table 5.1 A summary of the simplest possible undex features a general numerical simulation should be able to model.

Phenomena	Benchmark
Free–field bubble motion	Characteristics described by the empirical relations in Sec. 3.2. Jet formation for bubbles with large buyoancy parameter δ.
Free–field initial shockwave Subsequent pressure waves	Described by the similitude equations in Sec. 3.1.
Repulsion from free surface	(γ, δ) plot in Fig. 4.4.
Attraction to rigid surface	(γ, δ) plot in Fig. 4.4.
Attraction to inclined surface	Migration direction determined by Eq. (4.10).

To begin with, we will try to introduce the underlying principle underpinning the simulation model we have used in Impetus. Being a commercial software, it is unfortunately impossible to give an exact description of the code so a more general description must suffice.

Impetus is primarily a Finite Element code, used to describe non-linear mechanical problems where extreme loadings can lead to large deformations. The code was initially developed to model detonation of buried charges under vehicles, but has later grown to include many other uses. Impetus has much in common with Autodyn, but is better suited for certain problems, while at the same time lacking some of the opportunities in Autodyn (no Euler solver for instance).

One of the advantages of Impetus is that it has been explicitly written to run on GPUs. In many cases GPUs are able to calculate very much faster than CPUs. Additionally, Impetus has a unique particle model that can be used to model sand and air, and which is not affected by technical problems of the standard methods (interaction between Euler and Lagrangian grids) in Autodyn and similar codes.

At FFI the calculation part of Impetus is run on a dedicated server with a number of GPUs. This gives considerably larger computing power and speed than Autodyn on a normal PC. Pre- and post processing of the Impetus simulations are done on a normal PC. During the covid-19 pandemic, another server was added enabling the possibility of running unclassified simulations on the internet from home.

5.1 Smoothed–particle hydrodynamics

To model underwater explosions in Impetus we have used the so–called smoothed–particle hydrodynamics (SPH) model. The SPH method was originally developed for applications in astrophysics by Gingold and Monaghan [53] and independently by Lucy [54]. The general idea is rather simple. The computational domain is discretized into a finite number of interacting particles. Each particle occupies a small volume, and carries information about the relevant field variables such as position, velocity, density, and stress. The field variable of a specific particle is determined by a weighted interpolation of the surrounding neighbouring particles. The weighting function is called the kernel function, and determines the strength of the particle–particle interactions. A more detailed mathematical description is given in App. G.

Compared to the well–established boundary element method, there are relatively few works utilizing the SPH method to describe underwater explosions. Unlike the boundary–element method, an advantage of the SPH method is that it is meshless and does not rely on the potential flow theory. In principle, this means that it is possible to describe large deformations, such as jetting, of the gas bubble without any need of modifying the equations of motion. In addition, it should also be possible to describe bubble–structure interactions in a relatively straightforward manner. A relevant disadvantage of the SPH method is that there does not exist a standard way to enforce reflectionless boundary conditions.

5.2 Simulations of free–field bubble dynamics

To the best of our knowledge and at the time of writing, no one has attempted to model underwater explosions in Impetus before this report. The problem was therefore very challenging and we were lucky to receive good support directly from the Impetus development team. We attempted a lot of different approaches, some of which did not go as planned. In the report we only include the approaches that we consider successful. During our numerous attempts at modeling undex phenomena, we discovered several bugs in the code which, with the help of the developers, have now been corrected.

In the following sections we compute the time dependence of the period and radius in Impetus and compare them to the empirical expressions discussed in section 3.2. For convenience, we restate the empirical relations here:

$$R_m = J\left(\frac{W}{Z+10}\right)^{1/3}, \quad \text{and,} \quad T = K\frac{W^{1/3}}{(Z+10)^{5/6}}. \tag{5.1}$$

5.2.1 Coupled smoothed–particle hydrodynamics and finite element method

In the numerical simulation we consider a spherical TNT charge placed at a various water depths Z. The water surrounding the charge is discretized into a finite element (FE) mesh, with a cylindrical cavity that is filled with SPH particles. The TNT charge is located at the centre of the cavity. The finite element mesh is smooth close to the cylindrical cavity, and more coarse further away from it. The geometry is shown in Fig. 5.1, and the material parameters are specified in Table 5.2.

To begin with, the goal is to calculate the time period and maximum radius during the first bubble pulse, and check if there is a correspondence with Eq. (5.1). To this end we run simulations utilizing spherical TNT charges with radius $r = 0.5\,\text{m}$ at various depths Z. For each simulation

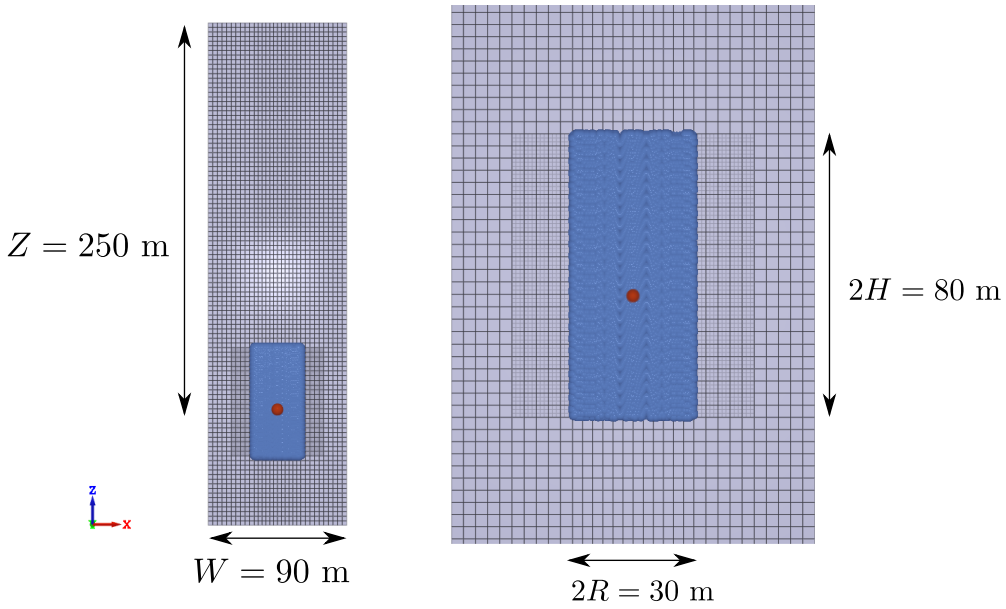

Figure 5.1 *The cross section of the geometry used to verify Eqs.* (5.1). *A spherical TNT charge (red), is embedded in a sea of SPH particles (blue), which are surrounded by a water FE mesh (lightblue). Close to the SPH particles the FE mesh is more smooth. Both the FE mesh, and SPH particles have cylindrical form. Gravity is acting in the $-z$ direction.*

Table 5.2 *The material parameters used in the numerical simulations. Note that there are several other parameters that are automatically specified in the input commands, which we do not include here.*

	TNT charge	SPH water	FE water
Density [kg/m^3]	1630	10^3	10^3
Particle number	-	10^7	-
Viscosity [mPa s]	-	1	1
Linear bulk modulus [GPa]	-	2.1	2.1

we plot the bubbles thermal energy as a function of time, and read off the first time period. An example of the thermal energy, as well as the vertical bubble migration is shown in Fig. 5.2, for an initial depth of $Z = 225$ m. The results look physically reasonable. The thermal energy oscillates with decaying amplitude as the bubble looses energy during each pulsation. The bubble migrates vertically the fastest when the bubble is small, and the slowest when the bubble is large.

Figure 5.3 compares the bubble dynamics modelled in Impetus with the well–known empirical relations. The continuous line represents the empirical expressions, and the dots represent individual simulations. As expected, the correspondence is not exact, but the scaling of the period and radius with the appropriate charge–depth ratio seems to be effectively captured in the simulations. Some of the reasons for the lack of a complete correspondence could be:

1. The empirical expressions are not themselves exact. Since the experiments are dated and not

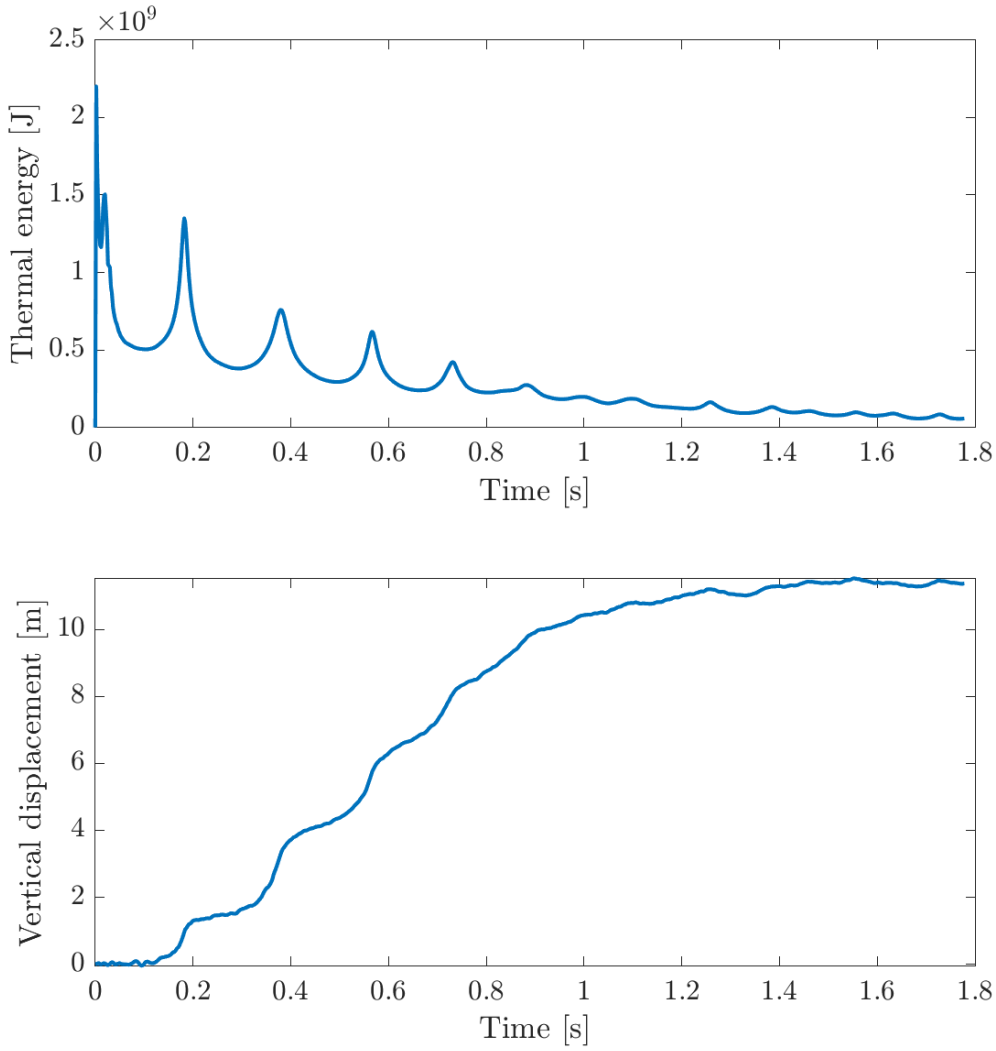

Figure 5.2 *The time dependence of the thermal energy and vertical bubble displacement for a charge located at an initial depth of 225 m below the water surface. Over time the thermal energy oscillates and dampens with the bubble dynamics. The bubble is migrating slowly when it is large, and quickly when it is small.*

easily accessible from open sources, it is hard to evaluate their experimental uncertainty.

2. In the simulations there is an artificial impedance mismatch between the SPH and FE region, which causes unphysical pressure–wave reflections at the interface between the two regions, see Fig. 5.4. To minimize the effect of this issue, a relatively large SPH region has been utilized so that the pressure–waves become geometrically damped before they are artificially reflected at the interface.
3. Since the bubble shrinks with time, the water mesh has a tendency to become inverted close to the SPH water particles during subsequent pulsations. Consequently, when the elements

become too inverted the simulation does not produce reliable results.

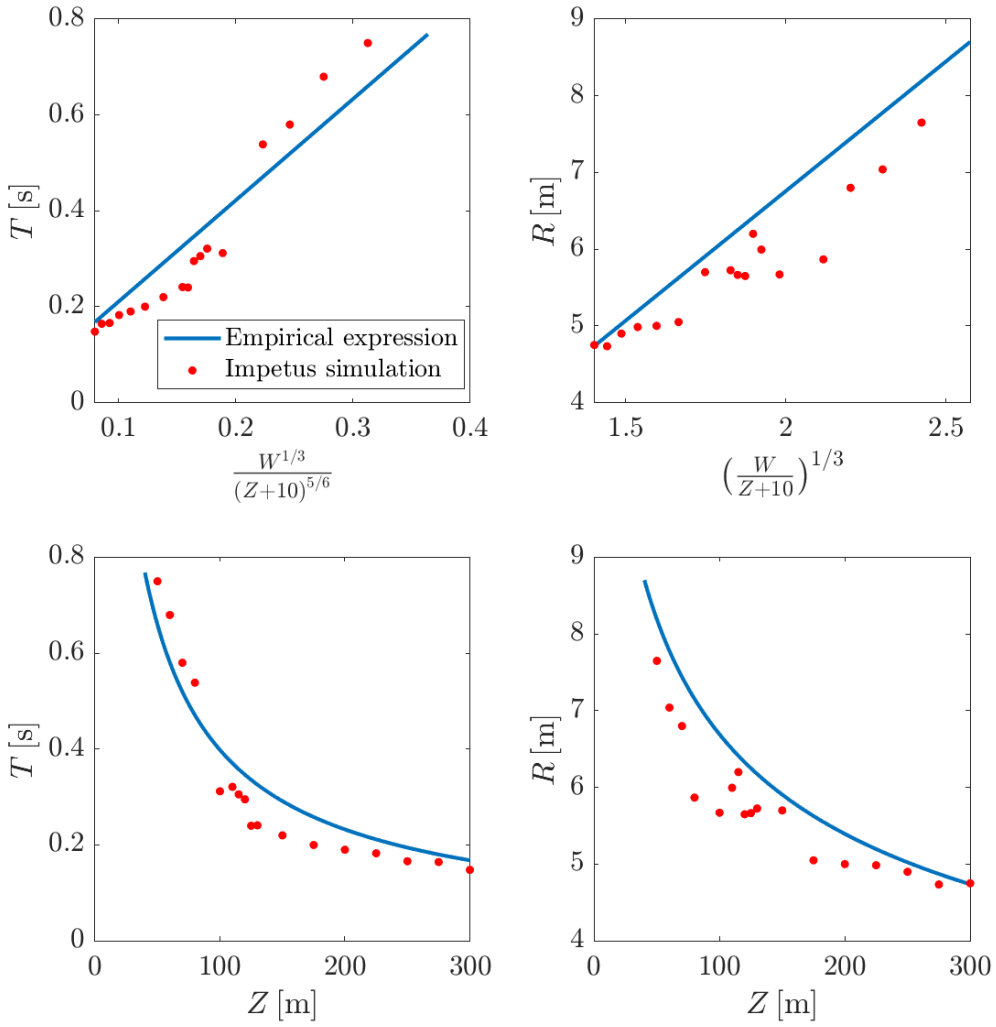

Figure 5.3 *A comparison of the bubble dynamics, for the first oscillation, modelled in Impetus and the empirical relations in Eq.* (5.1)*. The radius is the most uncertain because it is not well defined in a particle simulation.*

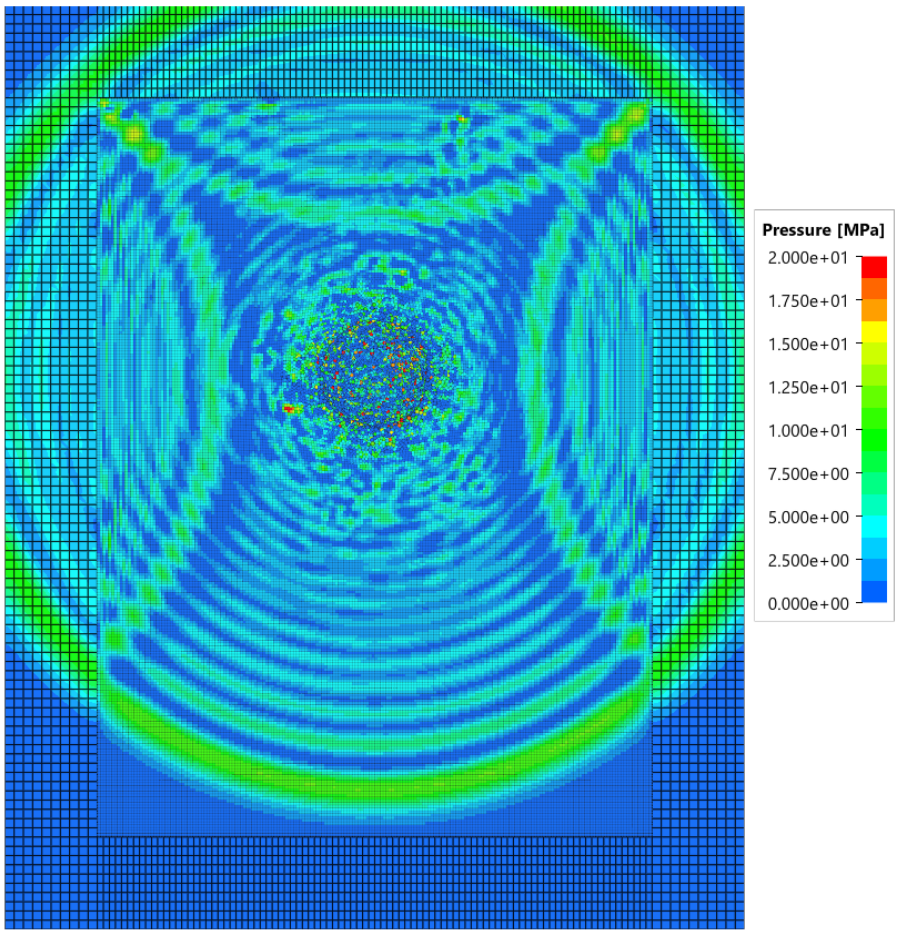

Figure 5.4 The impedance mismatch at the interface between the SPH region and FE mesh results in unphysical pressure–wave reflections.

5.2.2 Pure SPH simulation

We have also attempted to model the undex using only the built in SPH algorithm, without any FE mesh. The idea was that this removes the unphysical reflections due to the impedance mismatch between the SPH region and FE mesh, as well as the issues associated with the mesh becoming inverted for subsequent pulsations. Yet, the boundary of the SPH domain acts as a rigid wall which again leads to reflections. In an attempt to circumvent this issue we have utilized a geometry with various layers of particle density, as shown in Fig. 5.5a. The idea is to have a high particle density in important areas and low density where not much is expected to happen, thus enabling us to model a larger domain without needing more particles.

The result of the simulation for an undex at an initial depth of 50 m is shown in Figs. 5.5a–5.5i. In total, the particle domain is $400\,\mathrm{m} \times 400\,\mathrm{m} \times 250\,\mathrm{m}$, and filled with 10^7 particles. Overall there is good qualitative agreement, and the method is able to simulate subsequent pulsations well. The method is not perfect, as there are quantitative discrepancies between the simulations and the empirical formula. The period is strongly dependent on the domain size, and at the time of writing the in–house GPU does not have enough memory to perform a calculation in larger regimes where we expect the period to converge to the empirical expression in Eq. (5.1).

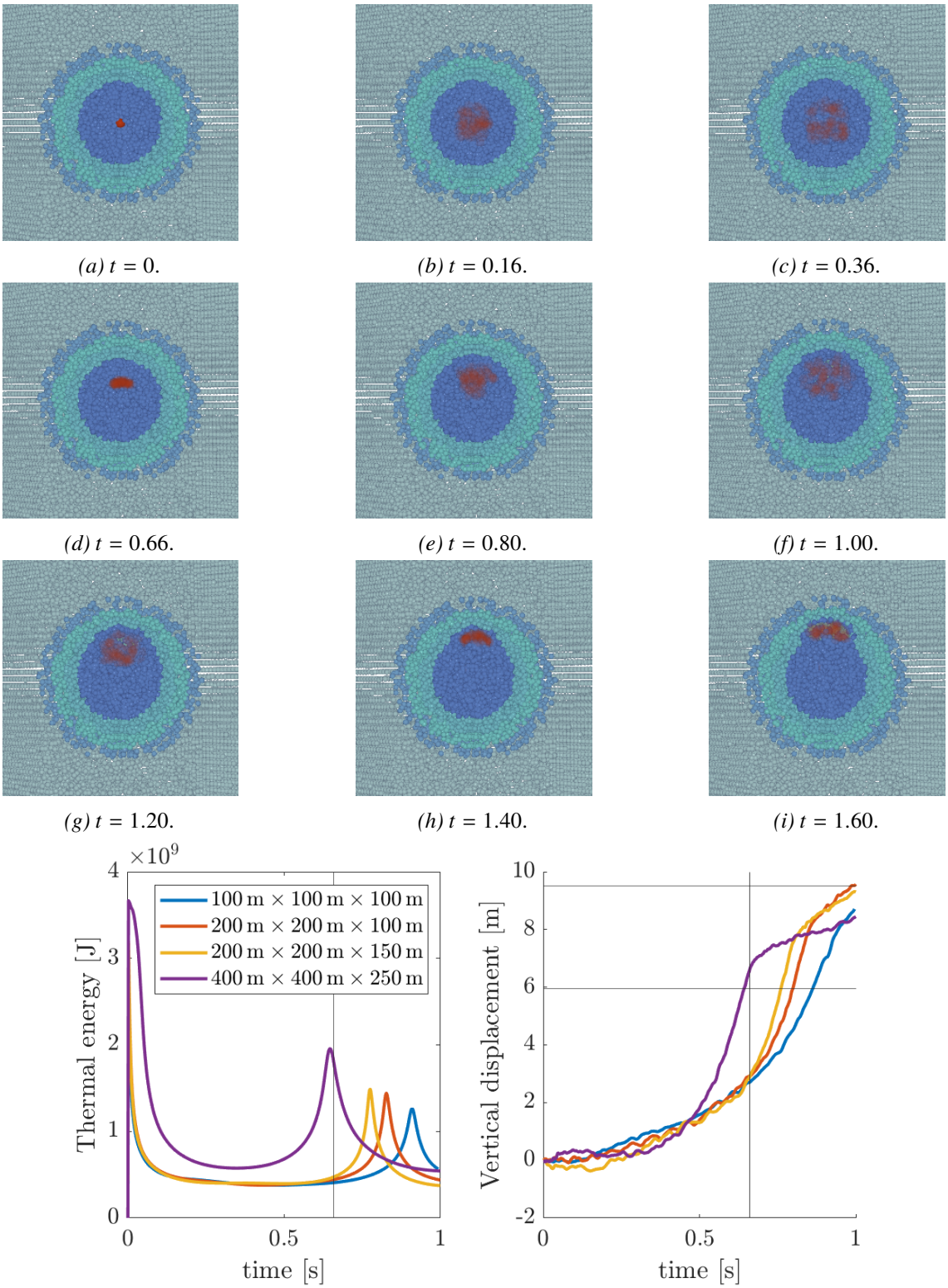

(a) $t = 0$. *(b)* $t = 0.16$. *(c)* $t = 0.36$.

(d) $t = 0.66$. *(e)* $t = 0.80$. *(f)* $t = 1.00$.

(g) $t = 1.20$. *(h)* $t = 1.40$. *(i)* $t = 1.60$.

(j) Thermal energy and bubble migration as a function of time.

Figure 5.5 Simulation of an undex at a depth of 50 m*, using only the SPH method. The TNT explosive (red) is surrounded by three spherical and two cubical SPH layers (blue and gray). As the domain size increases, the numerical simulations seems to converge towards the theoretical period and bubble migration. The theoretical values are drawn as horizontal and vertical lines respectively.*

5.3 Simulation of free–field shockwave propagation

Figure 5.6 shows the propagation of the initial shock wave from a detonation where we have detonated a spherical TNT charge of radius 0.5 m at a depth of 50 m below the water surface. The domain size is 100 m × 100 m × 100 m. The qualitative behaviour, displayed in Figs. 5.6a–5.6d, of the shock seems physical:

- The shockwave becomes geometrically damped as it propagates through the water.
- The reflection from the free surface produces a rarefaction wave carrying an under–pressure.
- The reflections from the rigid surfaces produces shockwaves carrying an over–pressure.

Unfortunately, the shockwave amplitude is significantly smaller than the empirical expression

$$p(\mathbf{r}, t) = p_m e^{-t/\theta} \tag{5.2}$$

predicts, as shown in Fig. 5.6e. In addition, the shape of the pressure waves are more reminiscent of large acoustic waves than actual shock waves. A discussion with the developer has indicated that this feature might be a resolution issue. This is supported quantitively by the fact that the impulse of the large acoustic wave seems to be similar to the expected impulse of the shockwave. Since the shockwaves are extremely thin a very high particle density is required, to completely resolve their singular features. Currently, the in–house GPUs are unable to model the necessary particle densities to obtain complete convergence.

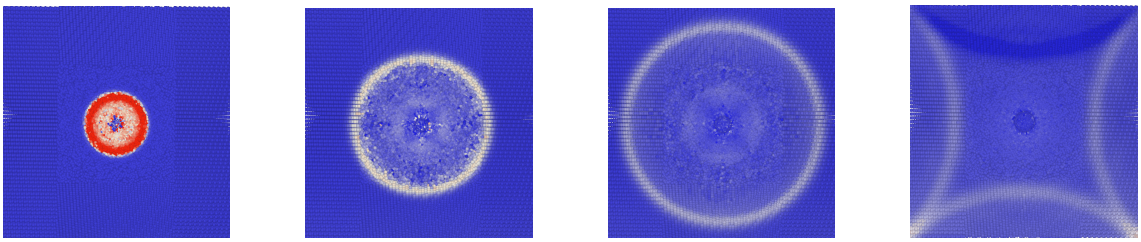

(a) $t = 8.0\,\text{ms}$. *(b)* $t = 19.0\,\text{ms}$. *(c)* $t = 29.0,\text{ms}$. *(d)* $t = 49.0\,\text{ms}$.

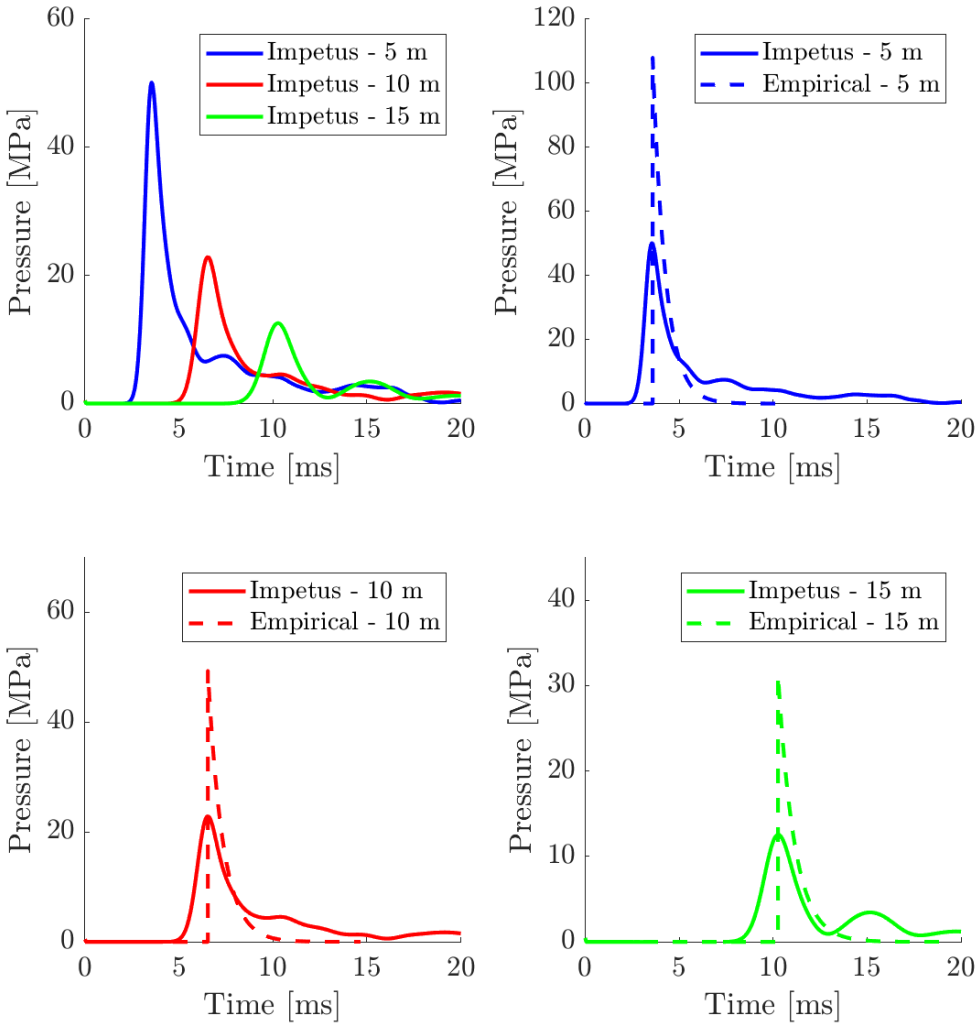

(e) Pressure history at the stand-off distances $r = 5\,\text{m}$, $r = 10\,\text{m}$, *and* $r = 15\,\text{m}$.

Figure 5.6 Simulation of the shockwave originating from a 852.5 kg *TNT charge placed* 50 m *below the water surface. The top boundary has a free boundary condition, the remaining ones have rigid boundary conditions.*

5.4 Summary

In this chapter we have attempted to model the free–field underwater explosion in Impetus, a summary is given in Fig. 5.7. Given that Impetus was not built with undex applications in mind, the results are better than expected, but not perfect. We have attempted two modeling strategies. In the first method, the region close to the explosive is discretized by SPH particles and the region far from the explosive is discretized by a mesh. We found however, that the mesh quickly becomes distorted for subsequent oscillations and that the interface between the mesh and SPH region causes unphysical reflections due to an impedance mismatch, see Fig. 5.4. In short, this modeling strategy limits the opportunities to either small bubbles, or only the first pulsation of large bubbles where the deformation of the mesh is minimal. That being said, the period and maximum radius for the first pulsation are in agreement with the corresponding empirical expressions, as shown in Fig. 5.3.

To avoid the issues associated with the mesh, we also attempted a second modeling strategy where we only utilized SPH particles. Simulations of the bubble dynamics seems to give physically reasonable results. We find that the bubble performs damped oscillations, with symmetric expansion and asymetric collapse. However, we do find that the period and radius depends on the size of the domain. A complete convergence to the empirical results therefore requires a very large domain size which is computationally expensive. Nevertheless, for large domains the simulations do come very close to the empirical results as shown in Fig. 5.5. Another issue, is that the pure SPH method also does not allow for reflectionless boundary conditions which means that reflected pressure waves may affect the bubble dynamics. We emphasize that this is a general disadvantage of the SPH method, not a flaw in the Impetus software.

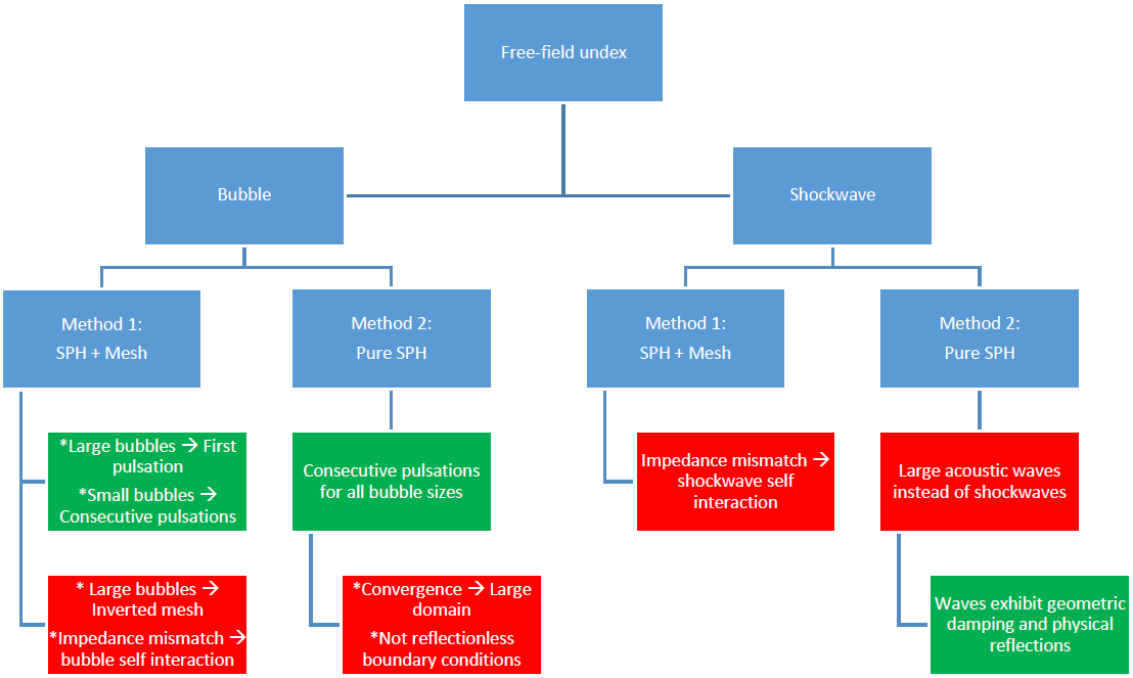

Figure 5.7 A graphic summary of the phenomena we have attempted to model. Green colors indicate successful modeling, and red colors indicate that there are issues which makes the modeling difficult or untrustworthy.

The description of the shockwave also has benefits and issues. The main issue is that Impetus is not able to completely resolve the shockwaves, without having an unattainable (at least for our GPUs) large particle density. Consequently, the shockwaves behave as large acoustic waves as shown in Fig. 5.6. The justification is that since the shockwaves are almost discontinuous it is easier to model large acoustic waves with similar impulse to the corresponding shockwave. On the other hand, Impetus seems to be able to handle the reflection properties of the acoustic wave well. Concretely, waves reflected off rigid surfaces come back as waves of overpressure and those reflected off free surfaces come back as waves of underpressure.

5.5 Possible solutions

With a bit of code development we propose two ways to circumvent the issues related to the lack of reflectionless boundary conditions. The first, is the introduction of ghost particles that live outside the water domain, close to the desired boundary, and interacts appropriately with the water SPH particles. The second, involves pausing the simulation as the shockwave reaches the boundary, removing the shockwave, and resuming the simulation with an appropriate initial condition on the water domain.

Another approach, may be to abandon the SPH description of the water, and instead introduce a new discrete water particle, through a new appropriately defined PARTICLE_WATER keyword. This may manifest similarly to the explosive (PARTICLE_HE), soil (PARTICLE_SOIL), and air (PARTICLE_AIR) particles already implemented in the code. This proposal is primarily motivated by the shape of the pressure histories in Fig. 5.6e, where the shape of the shockwave seems more reminiscent of large acoustic waves, which may indicate an issue with the compressibility of water in the current SPH description or be consequence of a resolution issue.

In addition, the Impetus team is currently working on developing a general CFD solver for air blast problems. At the time of writing the prototype seems to work well. That being said, the prototype only uses the Jones–Wilkins–Lee equations of state for the explosive and ideal gas equation for air, which are the simplest possible choices. If the development continues to be successful, we are also going to test the new solver for the application of undex problems. We believe that the procedure will allows us to model larger water domains without being too computationally expensive.

6 Conclusion

The first part of this report consists of a detailed literature study of the simplest underwater explosion phenomena. We have primarily focused on pressure characteristics through the similitude equations, and the bubble pulsation. References that contain data that could be useful for numerical benchmarking purposes have been included. In addition, the simplest forms of bubble–structure interaction has been discussed.

In the second part of this report we attempted to model undex using the numerical code Impetus. Given that the Impetus code has not primarily been developed for such applications, the results were better than expected. In general, Impetus are able to capture the qualitative features of free–field bubble motion and shockwave propagation. However, it remains to demonstrate quantitative convergence towards empirical relationships, as the bubble motion was seen to depend strongly on domain size and boundary conditions. For the shockwave, Impetus was also able to capture the most important qualitative features, while there was still some discrepancy for the amplitude and shape of the shock wave.

Finally, we provide a list, see Tab. 6.1, of the undex phenomena modelled in this report. We have highlighted in color which phenomena we have attempted to model and whether they have been successful or not. In addition, there are included several long–term effects that the FFI hopes the Impetus code will be able to model in the future. Given a continued close conversation with the developer we are confident many of these phenomena will be implemented in the hopefully not–too–distant future. To be concrete, the list includes specific simulation setups and experimental data useful for benchmarking.

Table 6.1 Starting points for undex phenomena that FFI is interested in modeling in Impetus. Green colors indicate that the phenomena has been modeled in this report, gray indicates that it will be modelled in a future report.

Short term		
Phenomena	*Setup*	*Benchmark*
Free–field bubble motion	Free–field charge	Characteristics described by the empirical relations in Sec. 3.2. Jet formation for bubbles with large buyoancy parameter δ.
Free–field initial shockwave Subsequent pressure waves	Free–field charge	Described by the similitude equations in Sec. 3.1.
Repulsion from free surface	Horizontal free surface above charge	(γ, δ) plot in Fig. 4.4.
Attraction to rigid surface	Horizontal rigid surface below charge	(γ, δ) plot in Fig. 4.4.
Attraction to rigid surface	Inclined rigid surface next to charge	Migration direction Eq. (4.10).

Long term		
Ship–shock interaction (Including reflections)	Target floating above charge,proximity to free and rigid surface	W. D. Reid [11]
Ship–bubble interaction (Cavitation, lift, whipping)	Target floating above charge (long stand–off)	G. Chertock [55, 56]
Jet–ship interaction (Water hammer)	Target floating above charge (Short stand–off)	S. M. Plesset [57] & T. J. Benjamin [58]
Bubble–submarine interaction	Submerged cylinder below charge	J. M. Brett [13]

References

[1] R. Kiciński and B. Szturomski. Pressure Wave Caused by Trinitrotoluene (TNT) Underwater Explosion—Short Review. *Applied Sciences 2020, Vol. 10, Page 3433*, 10:3433, 5 2020.

[2] R. H. Cole. *Underwater explosions*. Princeton University Press, 1948.

[3] S. Rosseland. Underwater explosion research. Technical Report S-RF 67, Norwegian Defence Research Establishment (FFI), 1950.

[4] S. Rosseland. The motion of the water following a submarine explosion. Technical Report S-RF 68, Norwegian Defence Research Establishment (FFI), 1950.

[5] J. H. Kiran. Undervannsdetonasjoner - en kort innføring (in norwegian). Technical Report 16/01500, Norwegian Defence Research Establishment (FFI), 2016.

[6] A. N. Osnes. Modeling underwater explosions: Extending charles to fiver. Technical Report 21/00963, Norwegian Defence Research Establishment (FFI), 2021.

[7] P. T. K. Østby, A. N. Osnes, and M. Vartdal. Simulation of underwater explosions using a simplified ghost fluid model: extending the fiver method to 3d. Technical Note 21/02232, Norwegian Defence Research Establishment (FFI), 2021.

[8] J. G. Kirkwoord and H. A. Bethe. Progress report on the pressure wave produced by an underwater explosion. Technical Report 4814, Office of Scientific Research and Development (OSRD), 1942.

[9] Jacob Sanders, Girum Urgessa, and Rainald Löhner. Literature review on the response of concrete structures subjected to underwater explosions. *CivilEng*, 2(4):895–908, 2021.

[10] M. Swizdak. Explosion effects and properties: part ii - explosion effects in water. Technical Report TR-76-116, Naval Surface Weapons Center, 1978.

[11] W. D. Reid. The response of surface ships to underwater explosions. Technical Report DSTO-GD-0109, Defence Science and Technology Organisation (DSTO), 1997.

[12] E. Klaseboer, K. C. Hung, C. Wang, C. W. Wang, B. C. Khoo, P. Boyce, S. Debono, and H. Charlier. Experimental and numerical investigation of the dynamics of an underwater explosion bubble near a resilient/rigid structure. *Journal of Fluid Mechanics*, 537:387–413, 2005.

[13] J. M. Brett and G. Yiannakopolous. A study of explosive effects in close proximity to a submerged cylinder. *International Journal of Impact Engineering*, 35(4):206–225, 2008.

[14] C. F. Hung and J. J. Hwangfu. Experimental study of the behaviour of mini-charge underwater explosion bubbles near different boundaries. *Journal of Fluid Mechanics*, 651:55–80, 2010.

[15] A. M. Zhang, S. P. Wang, C. Huang, and B. Wang. Influences of initial and boundary conditions on underwater explosion bubble dynamics. *European Journal of Mechanics - B/Fluids*, 42:69–91, 2013.

[16] P. Cui, A. M. Zhang, and S. P. Wang. Small-charge underwater explosion bubble experiments under various boundary conditions. *Physics of Fluids*, 28(11):117103, 2016.

[17] S. Li, A. M. Zhang, R. Han, and P. Cui. Experimental and numerical study of two underwater explosion bubbles: Coalescence, fragmentation and shock wave emission. *Ocean Engineering*, 190:106414, 2019.

[18] S. Wang, Q. Gui, J. Zhang, Y. Gao, J. Xu, and X. Jia. Theoretical and experimental study of bubble dynamics in underwater explosions. *Physics of Fluids*, 33(12):126113, 2021.

[19] Lord Rayleigh. On the pressure developed in a liquid during the collapse of a spherical cavity. *The London, Edinburgh, and Dublin Philosophical Magazine and Journal of Science*, 34(200):94–98, 1917.

[20] M. S. Plesset. The Dynamics of Cavitation Bubbles. *Journal of Applied Mechanics*, 16(3):277–282, 04 1949.

[21] H. Lamb. The early stages of a submarine explosion. *The London, Edinburgh, and Dublin Philosophical Magazine and Journal of Science*, 45(266):257–265, 1923.

[22] E. L. Lee, H. C. Hornig, and J. W. Kury. Adiabatic expansion of high explosive detonation products. Technical Report UCRL-50422, University of California, Lawrence Radiation Laboratory, Livermore, CA, USA, 1968.

[23] C. E. Brennen. *Cavitation and bubble dynamics*. Oxford University Press, 1995.

[24] I. I. Kolodner and J. B. Keller. Underwater Explosion Bubbles I: The Effect of Compressibility of the Water. Technical Report Nonr-285 (02), Office of Naval Research, 1953.

[25] J. B. Keller and I. I. Kolodner. Damping of underwater explosion bubble oscillations. *Journal of Applied Physics*, 27(10):1152–1161, 1956.

[26] C. Herring. Theory of the pulsations of the gas bubble produced by an underwater explosion. Technical Report C4-sr20, National Defense Research Committee (NDRC), 1941.

[27] GI Taylor. The vertical motion of a spherical bubble and the pressure surrounding it. Technical report, David Taylor Model Basin – Acoustics and Vibration Lab, 1943.

[28] F. R. Gilmore. The growth or collapse of a spherical bubble in a viscous compressible liquid. Technical Report 26-4, California Institute of Technology, Hydrodynamics Laboratory, 1952.

[29] I. I. Kolodner and J. B. Keller. Underwater Explosion Bubbles II: The Effect of Gravity and Change of Shape. Technical Report Nonr-285 (02), Office of Naval Research, 1953.

[30] A. Prosperetti and A. Lezzi. Bubble dynamics in a compressible liquid. part 1. first-order theory. *Journal of Fluid Mechanics*, 168:457–478, 1986.

[31] A. Lezzi and A. Prosperetti. Bubble dynamics in a compressible liquid. part 2. second-order theory. *Journal of Fluid Mechanics*, 185:289–321, 1987.

[32] T. L. Geers and K. S. Hunter. An integrated wave-effects model for an underwater explosion bubble. *The Journal of the Acoustical Society of America*, 111(4):1584–1601, 2002.

[33] J. R. Blake, G. Doherty, and B. B. Taib. Transient cavities near boundaries. part 1. rigid boundary. *Journal of Fluid Mechanics*, 170:479–497, 1986.

[34] J. R. Blake, B. B. Taib, and G. Doherty. Transient cavities near boundaries part 2. free surface. *Journal of Fluid Mechanics*, 181:197–212, 1987.

[35] J. R. Blake. The kelvin impulse: application to cavitation bubble dynamics. *The Journal of the Australian Mathematical Society. Series B. Applied Mathematics*, 30(2):127–146, 1988.

[36] J. R. Blake and P. Cerone. A note on the impulse due to a vapour bubble near a boundary. *The Journal of the Australian Mathematical Society. Series B. Applied Mathematics*, 23(4):383–393, 1982.

[37] J. P. Best. *The dynamics of underwater explosions*. PhD thesis, University of Wollongong, Department of mathematics, 1991.

[38] J. P. Best and J. R. Blake. An estimate of the kelvin impulse of a transient cavity. *Journal of Fluid Mechanics*, 261:75–93, 1994.

[39] J. R. Blake, D. M. Leppinen, and Q. Wang. Cavitation and bubble dynamics: the kelvin impulse and its applications. *Interface Focus*, 5(5):20150017, 2015.

[40] E. Klaseboer, B. C. Khoo, and K. C. Hung. Dynamics of an oscillating bubble near a floating structure. *Journal of Fluids and Structures*, 21:395–412, 12 2005.

[41] Y. L. Zhang, K. S. Yeo, B. C. Khoo, and C. Wang. 3d jet impact and toroidal bubbles. *Journal of Computational Physics*, 166:336–360, 1 2001.

[42] Shi-Min Li, A-Man Zhang, and Nian-Nian Liu. Effect of a rigid structure on the dynamics of a bubble beneath the free surface. *Theoretical and Applied Mechanics Letters*, page 100311, 12 2021.

[43] Ming He, A. Man Zhang, and Yun Long Liu. Prolonged simulation of near-free surface underwater explosion based on eulerian finite element method. *Theoretical and Applied Mechanics Letters*, 10:16–22, 1 2020.

[44] M. B. Liu, G. R. Liu, K. Y. Lam, and Z. Zong. Smoothed particle hydrodynamics for numerical simulation of underwater explosion. *Computational Mechanics 2003 30:2*, 30:106–118, 2003.

[45] Tieshuan Zhuang and Xiangwei Dong. Smoothed particle hydrodynamics simulation of underwater explosions with dynamic particle refinement. *AIP Advances*, 10:115314, 2020.

[46] A. M. Zhang, W. B. Wu, Y. L. Liu, and Q. X. Wang. Nonlinear interaction between underwater explosion bubble and structure based on fully coupled model. *Physics of Fluids*, 29:082111, 8 2017.

[47] Zhi Zong, Jia xia Wang, Li Zhou, and Gui yong Zhang. Fully nonlinear 3d interaction of bubble dynamics and a submerged or floating structure. *Applied Ocean Research*, 53:236–249, 10 2015.

[48] A. Man Zhang, Shi Ping Wang, Chao Huang, and Bin Wang. Influences of initial and boundary conditions on underwater explosion bubble dynamics. *European Journal of Mechanics - B/Fluids*, 42:69–91, 11 2013.

[49] Zhi Fan Zhang, Cheng Wang, A. Man Zhang, Vadim V. Silberschmidt, and Long Kan Wang. Sph-bem simulation of underwater explosion and bubble dynamics near rigid wall. *Science China Technological Sciences*, 62:1082–1093, 7 2019.

[50] A. M. Zhang, F. R. Ming, and S. P. Wang. Coupled sphs–bem method for transient fluid–structure interaction and applications in underwater impacts. *Applied Ocean Research*, 43:223–233, 10 2013.

[51] Tong Li, Shiping Wang, Shuai Li, and A. Man Zhang. Numerical investigation of an underwater explosion bubble based on fvm and vof. *Applied Ocean Research*, 74:49–58, 5 2018.

[52] Yunlong Liu, A. Man Zhang, Zhaoli Tian, and Shiping Wang. Investigation of free-field underwater explosion with eulerian finite element method. *Ocean Engineering*, 166:182–190, 10 2018.

[53] R. A. Gingold and J. J. Monaghan. Smoothed particle hydrodynamics: theory and application to non-spherical stars. *Monthly Notices of the Royal Astronomical Society*, 181(3):375–389, 1977.

[54] L. B. Lucy. A numerical approach to the testing of the fission hypothesis. *The Astronomical Journal*, 82(12):1013–1024, 1977.

[55] G. Chertock. Transient Flexural Vibrations of Ship-Like Structures Exposed to Underwater Explosions. *The Journal of the Acoustical Society of America*, 48(1B):170–180, 1970.

[56] G. Chertock. The Flexural Response of a Submerged Solid to a Pulsating Gas Bubble. *Journal of Applied Physics*, 24(2):192–197, 1953.

[57] Milton S. Plesset and Richard B. Chapman. Collapse of an initially spherical vapour cavity in the neighbourhood of a solid boundary. *Journal of Fluid Mechanics*, 47(2):283–290, 1971.

[58] T. B. Benjamin, A. T. Ellis, and Frank Philip Bowden. A discussion on deformation of solids by the impact of liquids, and its relation to rain damage in aircraft and missiles, to blade erosion in steam turbines, and to cavitation erosion - the collapse of cavitation bubbles and the pressures thereby produced against solid boundaries. *Philosophical Transactions of the Royal Society of London. Series A, Mathematical and Physical Sciences*, 260(1110):221–240, 1966.

[59] T. L. Geers and C. K. Park. Optimization of the G & H Bubble Model. *Shock and Vibration*, 12(1):3–8, 2005.

[60] N. N. Liu, A. M. Zhang, P. Cui, S. P. Wang, and S. Li. Interaction of two out-of-phase underwater explosion bubbles. *Physics of Fluids*, 33(10):106103, 2021.

[61] Yen C. Huang, F. G. Hammitt, and T. M. Mitchell. Note on shock-wave velocity in high-speed liquid-solid impact. *Journal of Applied Physics*, 44(4):1868–1869, 1973.

[62] E. Johnsen and T. Colonius. Numerical simulations of non-spherical bubble collapse. *Journal of Fluid Mechanics*, 629:231–262, 2009.

A Derivation of the similitude equations

In this appendix, we wish to show that the equations of motion

$$\begin{aligned} &\frac{\mathrm{d}\rho}{\mathrm{d}t} + \rho\nabla\cdot\mathbf{v} = 0, \quad \text{Mass,} \\ &\rho\frac{\mathrm{d}\mathbf{v}}{\mathrm{d}t} + \nabla p = 0, \quad \text{Momentum,} \\ &\rho\frac{\mathrm{d}}{\mathrm{d}t}\left(E + \frac{1}{2}\mathbf{v}^2\right) + \nabla(p\mathbf{v}) = 0, \quad \text{Energy,} \end{aligned} \tag{A.1}$$

and the Rankine-Hugoinot relations

$$\begin{aligned} &\rho\,(U-u) = \rho_0 U, \quad \text{Mass,} \\ &p - p_0 = \rho_0 U u, \quad \text{Momentum,} \\ &E - E_0\frac{1}{2}\rho_0 U u, \quad \text{Energy,} \end{aligned} \tag{A.2}$$

governing the bulk fluid and shockwave properties respectively, are invariant under the simultaneous scaling of space and time of the form $(\mathbf{r}, t) \to (\lambda\mathbf{r}, \lambda t)$, where λ is a scalar. For the Rankine–Hugoinot relations the scale invariance is trivial because there are no derivatives. In the equations of motion this is a consequence of all the derivatives having the same order. We will illustrate the scale invariance by considering the conservation of momentum, but emphasize that all Eqs. in (A.1) and (A.2) exhibit the same scale invariance. By writing $\mathbf{r}' = \lambda\mathbf{r}$ and $t' = \lambda t$ we obtain

$$\rho\frac{\mathrm{d}\mathbf{v}(\mathbf{r}', t')}{\mathrm{d}t'} = -\nabla' p(\mathbf{r}', t') \tag{A.3}$$

where the prime indicates differentiation with respect to the scaled coordinates. Since, all the derivatives have the same order we can simplify to

$$\rho\frac{\mathrm{d}\mathbf{v}(\lambda\mathbf{r}, \lambda t)}{\mathrm{d}t} = -\nabla p(\lambda\mathbf{r}, \lambda t), \tag{A.4}$$

and observe that scale invariance is now manifest.

The similitude equations follow from the principle of similarity by choosing $\lambda = 1/a_0$ where a_0 is a length scale, for instance the radius, characterizing the charge. In the following $f(\cdot)$, $g(\cdot)$, $h(\cdot)$, and $u(\cdot)$ denote arbitrary functions. With this choice it follows that space and time must scale like $\mathbf{r}/a_0$ and t/a_0 respectively. If we then consider a shockwave which has reached the point $\mathbf{r}$ at time $t = 0$ we can draw a few conclusions. The peak of the shockwave must take the form

$$p_m = f\left(\frac{a_0}{r}\right) \tag{A.5}$$

because it is time independent. It is natural[7] to consider that the shockwave decays exponentially in time, where the time scale is set by a time constant which we denote by θ. According to the principle of similarity the time constant must scale like

$$\frac{\theta}{a_0} = g\left(\frac{a_0}{r}\right). \tag{A.6}$$

[7] This is proved in the Kirkwood–Bethe theory [8] which is too involved to include here.

The impulse of the shockwave is defined as

$$I(r,t) = \int_0^{5\theta} p(\mathbf{r},\tau)\mathrm{d}\tau, \tag{A.7}$$

where the upper limit of integration (5θ) has been chosen by convention. The shockwave impulse can then be written as

$$\begin{aligned} I &= \int_0^{5\cdot g\left(\frac{a_0}{r}\right)a_0} p\left(\frac{a_0}{r},\frac{\tau}{a_0}\right)\mathrm{d}\tau \\ &= a_0\int_0^{5\cdot g\left(\frac{a_0}{r}\right)} p\left(\frac{a_0}{r},\frac{\tau}{a_0}\right)\mathrm{d}\left(\frac{\tau}{a_0}\right) \\ &= a_0 h\left(\frac{a_0}{r}\right). \end{aligned} \tag{A.8}$$

This demonstrates that the shockwave impulse scales like

$$\frac{I}{a_0} = h\left(\frac{a_0}{r}\right). \tag{A.9}$$

The derivation for the energy of the shockwave is very similar to the impulse, except for a constant prefactor and that $p(\mathbf{r},\tau)$ is replaced by $p^2(\mathbf{r},\tau)$ in the relevant integral, see Eq. (3.3). This leads to an identical scaling for the shockwave energy

$$\frac{E}{a_0} = u\left(\frac{a_0}{r}\right). \tag{A.10}$$

Equations (A.5), (A.6), (A.9), and A.10 represent the theoretical expressions for the shockwave similitude equations. However, in an experiment it is customary to choose the cube root of the explosive mass W instead of an actual length scale of the charge. First and foremost, this is because it is simpler to measure the mass of the explosive than either measuring the charge radius, or choosing an appropriate length scale for non–spherical charges. The cube root is related to that the mass W can be expressed as a product of charge density and charge volume, and the charge volume has dimensions of cubic length. Thus, to lowest order the similitude equations are conventionally expressed in the form

$$\text{Parameter} = K\left(\frac{W^{1/3}}{r}\right)^{\alpha}, \tag{A.11}$$

where K is a dimensional constant. The parameters K and α have been determined through numerous experiments, summarized in [2].

We now discuss some of the assumptions that underpin the similitude equations. We mentioned that the scale invariance of the equations of motion depends on the derivatives having the same order. In effect, this means that any term that depends on second (or higher) order derivatives will break the scale invariance. The prime example of such terms is the viscosity $\mu\nabla^2\mathbf{v}$, and other dissipative forces such as heat conduction. It is speculated that also chemical reactions behind the detonation front may also violate the scale invariance. Note that, we have assumed the absence of boundaries. In fact the similitude equations are only valid in the free–field case. Another important force that does not scale geometrically, is the gravitational force. For shockwave dynamics gravity causes no problems, because the time scale of the event is so small that the acceleration of water due to gravity is negligible. At first sight, this may seem like a lot of assumptions that may be

violated. Nevertheless, we emphasize that the similitude equations seem to describe the shockwave physics in a fashion that agrees with experimental data.

Next, one might wonder if we also can use similitude equations to describe the bubble dynamics. The answer is yes, but the relevant scaling relations between time and space are different. This means that it is actually impossible to preserve both shockwave and bubble dynamics during the same scale transformation. The primary cause of the difference in scaling behavior is the gravitational acceleration. The time scale of the bubble dynamics is so long that gravity plays an important role in the dynamics, causing e.g. asymmetric bubble collapse and upwards bubble migration. Since the gravitational acceleration has dimensions of length/time^2, it follows that if the length is scaled by a factor λ, then time must be scaled with a factor $\sqrt{\lambda}$ in order to preserve the value of the gravitational acceleration during a scale transformation.

B Derivation of the Willis formula

In this section we derive Eq. (3.5). In the simplest approximation we assume that the bubble expansion keeps the density of water constant and only induces radial flow of the surrounding water. We also neglect the effect of gravity. With these assumptions our starting point is the equation of continuity

$$\frac{\partial u}{\partial r} = -\frac{2u}{r} \tag{B.1}$$

and motion

$$\rho_0 \frac{\partial u}{\partial t} + \rho_0 u \frac{\partial u}{\partial r} + \frac{\partial P}{\partial r} = 0 \tag{B.2}$$

in spherical coordinates. Integrating the equation of continuity we obtain $u(r,t) = u_1(t)/r^2$ where $u_1(t)$ is a time–dependent integration constant. By substituting this into the equation of motion we obtain

$$\frac{1}{r^2}\rho_0 + \frac{\mathrm{d}u_1}{\mathrm{d}t} + \frac{1}{2}\rho_0 \frac{\partial u^2}{\partial r} + \frac{\partial P}{\partial r} = 0. \tag{B.3}$$

We can now integrate from the surface of the gas sphere ($r = R$) to infinity ($r = \infty$), with the boundary conditions $u(r = R, t) = u_R = \mathrm{d}R/\mathrm{d}t = u_1/R$, $P(r = R) = P_R$, and $P(r = \infty) = P_0$ and $u(r = \infty, t) = 0$. If we then integrate with respect to time we obtain an expression for the conservation of energy

$$Y = \frac{3}{2}\left(\frac{4\pi}{3}\rho_0 R^3\right)\left(\frac{\mathrm{d}R}{\mathrm{d}t}\right)^2 + \frac{4\pi}{3}P_0 R^3 + E(R). \tag{B.4}$$

The first, second, and third term represents the kinetic energy, the work done against hydrostatic pressure, and the internal energy respectively. Concretely the internal energy is defined as

$$E(R) = \int_{V(R)}^{\infty} P\mathrm{d}V \tag{B.5}$$

and is therefore determined by the equation of state. Commonly it is assumed that the expansion is adiabatic, so that $P(V/W)^\gamma = k$. Here W is the mass of explosive products and k is a constant. It can be shown that the fraction of internal energy compared to the total energy is

$$F = \frac{E(R)}{Y} = 0.166 P_R^{1/5} = 0.42\left(\frac{W}{R^3}\right)^{1/4}. \tag{B.6}$$

Estimates suggests that as a first-approximation it is okay to neglect $E(R)$ compared to Y[8]. If we neglect $E(R)$ we can obtain a simple expression for the energy in terms of the maximal radius ($\mathrm{d}R/\mathrm{d}t = 0$):

$$Y = \frac{4\pi}{3}P_0 R_m^3. \tag{B.7}$$

Furthermore, by neglecting $E(R)$ in Eq. (B.4) we can use seperation of variables to obtain an expression for the time it takes to expand from an initial radius R_0 to an arbitrary radius $R(t)$

$$t = \left(\frac{3\rho_0}{2P_0}\right)^{1/2} \int_{R_0}^{R} \frac{\mathrm{d}R}{\left[\left(\frac{R_m}{R}\right)^3 - 1\right]^{1/2}}. \tag{B.8}$$

[8] at least the equations become simpler.

In the equation above we eliminated Y by utilizing Eq. (B.7). We can then obtain an expression for the period of oscillation by integrating from $R_0 = 0$ to $R = a_m$. The expression is called the Willis formula and takes the form

$$T = 1.83\, R_m \left(\frac{\rho_0}{P_0}\right)^{1/2} = 1.14\, \rho_0^{1/2} \frac{Y^{1/3}}{P_0^{5/6}}. \tag{B.9}$$

So the period varies as the cube root of the total energy or equivalently the explosive charge weight since $Y \propto W$. It also varies as the 5/6th root of the hydrostatic pressure, which is connected to the charge depth Z through the relation $P_0 \approx P_{atmosphere} + \rho_0 g Z$. Dimensional analysis suggests that despite our numerous approximations the depedence on $\rho_0^{1/2}$, $Y^{1/3}$, and $P_0^{5/6}$ is more general

$$T \propto \rho_0^{1/2} \frac{Y^{1/3}}{P_0^{5/6}}. \tag{B.10}$$

Experiments demonstrate that the formula is valid given that the approximate number 1.14 is adjusted suitably, which gives rise to the experimental relationship

$$T = K \frac{W^{1/3}}{(Z + 10)^{5/6}}. \tag{B.11}$$

Similarly Eq. (B.7) yields

$$R_m = J \left(\frac{W}{Z + 10}\right)^{1/3}. \tag{B.12}$$

Note that the constants K and J are now dimensional, because we utilized the relation $Y \propto W$.

C Lamb–Rayleigh–Plesset equation

C.1 Derivation

Consider an expanding or contracting spherical gas bubble of radius $R(t)$, immersed in a fluid. The fluid is specified by the space and time coordinates $(\mathbf{r}, t)$. In the following, we assume spherical symmetry so that the fluid velocity only has a radial component v_r. The pressure inside the bubble is p_b, the stress tensor in the fluid is $\boldsymbol{\sigma}$, and the intrinsic surface tension is denoted by γ. The force balance in the normal direction at the bubble interface is (evaluated at $r = R$)

$$\begin{aligned} 0 &= \sigma_{rr} + p_b - \gamma\,(\nabla \cdot \mathbf{n}) \\ &= \sigma_{rr} + p_b - \gamma\left(\frac{2}{R}\right) \end{aligned} \tag{C.1}$$

where, $\mathbf{n} = \hat{\mathbf{r}}$ denotes the unit normal of the bubble. To determine the equation of motion we need to determine the stress tensor in the fluid.

To derive the stress tensor of the fluid surrounding the bubble we make some simplifying assumptions. The density ρ and viscocity μ of the liquid are both constant, and we define the kinematic viscocity as $\nu = \mu/\rho$. Physically this means that we consider an incompressible fluid (infinite speed of sound), with finite viscosity. We also assume that the temperature and pressure inside the bubble is uniform.

Continuity at the bubble interface dictates that

$$v_r(r = R, t) = \frac{\mathrm{d}R}{\mathrm{d}t}. \tag{C.2}$$

If the flow is incompressible, then if the bubble expands the change in bubble volume should equal the change in fluid volume and therefore

$$v_r(r, t) = \frac{R^2}{r^2}\frac{\mathrm{d}R}{\mathrm{d}t} \equiv \frac{F^2(t)}{r^2}, \tag{C.3}$$

where we defined $F(t) = R^2\mathrm{d}R/\mathrm{d}t$.

In spherical coordinates the Navier–Stokes equation takes the form

$$\frac{\partial v_r}{\partial t} + v_r\frac{\partial v_r}{\partial r} = -\frac{1}{\rho}\frac{\partial p}{\partial r} + \nu\left\{\frac{1}{r^2}\left[\frac{\partial}{\partial r}\left(r^2\frac{\partial v_r}{\partial r}\right)\right] - \frac{2v_r}{r^2}\right\}. \tag{C.4}$$

If we substitute $v(r, t) = F^2(t)/r^2$ into the Navier–Stokes equation we obtain

$$-\frac{1}{\rho}\frac{\partial p}{\partial r} = \frac{1}{r^2}\frac{\mathrm{d}F}{\mathrm{d}t} - \frac{2}{r^5}F^2. \tag{C.5}$$

Note that due to the spherical symmetry the term proportional to the viscosity ν cancelled. Integrating Eq. (C.5) from $r = r$ to $r = \infty$ gives us an equation for the pressure profile in terms of the velocity field

$$\frac{p(r, t) - p_\infty}{\rho} = \frac{1}{r}\frac{\mathrm{d}F}{\mathrm{d}t} - \frac{F^2}{2r^4}. \tag{C.6}$$

In spherical coordinates the stress tensor is defined as

$$\begin{aligned}\sigma_{rr} &= -p + 2\mu\frac{\partial v_r}{\partial r} \\ &= -\left(p_\infty + \frac{\rho}{R}\frac{\mathrm{d}F}{\mathrm{d}t} - \frac{\rho}{2R^4}F^2\right) - \frac{4\mu F}{R^3},\end{aligned} \tag{C.7}$$

where we in the final line evaluated the stress tensor for $r = R$.

By substituting the stress tensor in Eq. (C.7) into the dynamic boundary condition in Eq. (C.1) we obtain the equation of motion

$$\frac{2\gamma}{R\rho} + R\ddot{R} + \frac{3}{2}\dot{R}^2 + 4\frac{\nu}{R}\dot{R} = \frac{p_b - p_\infty}{\rho}. \tag{C.8}$$

By introducing the bubble volume $V_B(t) = 4/3\pi R^3(t)$ we can rewrite Eq. (C.6) to obtain an expression for the pressure distribution in the surrounding liquid,

$$p(r,t) = p_\infty + \rho\left[\frac{\ddot{V}_B(t)}{4\pi r} - \frac{\dot{V}_B^2(t)}{32\pi^2 r^4}\right]. \tag{C.9}$$

C.2 Numerical solution

To obtain a numerical solution we need to specify the set of parameters $\{R_0, \dot{R}_0, p_\infty, k, K, \rho, \mu, \gamma\}$. In principle, this can be done by relying on empirical data, the validity of which is certainly questionable. Alternatively, we can reduce the number of necessary parameters by expressing the Lamb–Rayleigh–Plesset equation in dimensionless form. To this end, we set the length scale equal to the equilibrium radius $\bar{R}$ which is defined through the equation $p_b(R = \bar{R}) = p_\infty$, and introduce the corresponding timescale as $T = \bar{R}\left(\rho p_\infty^{-1}\right)^{1/2}$. The dimensionless radius, time, dynamic viscocity, and surface tension then takes the form

$$a = R/\bar{R}, \quad \tau = t/T, \quad M = \frac{\mu}{Tp_\infty}, \quad \text{and} \quad S = \frac{\gamma}{p_\infty \bar{R}} \tag{C.10}$$

respectively. Substituting the dimensionless variables in Eq. (C.10) into Eqs. (4.1) and (4.2), we obtain the dimensionless Lamb–Rayleigh–Plesset equation

$$a\ddot{a} + \frac{3}{2}\dot{a}^2 + 4M\frac{\dot{a}}{a} + \frac{2S}{a} = a^{-3K} - 1. \tag{C.11}$$

To solve the dimensionless Lamb–Rayleigh–Plesset equation we need only specify the parameters $\{a_0, \dot{a}_0, M, S, K\}$. The benefit of the dimensionless equation, is that we no longer need to specify the charge constant k which was the parameter with greatest empirical uncertainty.

To asses the validity of the dimensionless Lamb–Rayleigh–Plesset equation we will compare the radius–time curve with an empirical one given on p. 271, Fig. 8.1 in Cole's book [2]. The case is a 0.25 kg tetryl charge detonated 91.44 m below the water surface. From the data we estimated that the equilibrium bubble radius is $\bar{R} = 0.15$ m. The first maximum bubble radius is $R_{\max} = 0.45$ m, which corresponds to $a_{\max} = 3$ in our dimensionless units. We began the integration from the first maximum using $a_0 = 3$, $\dot{a}_0 = 0$, and $K = 1.25$. For water, the dimensionless viscocity and surface tension becomes $M = 2 \times 10^{-4}$, and $S = 4.7 \times 10^{-7}$ respectively. The solution as well as the empirical data is shown in Fig. C.1.

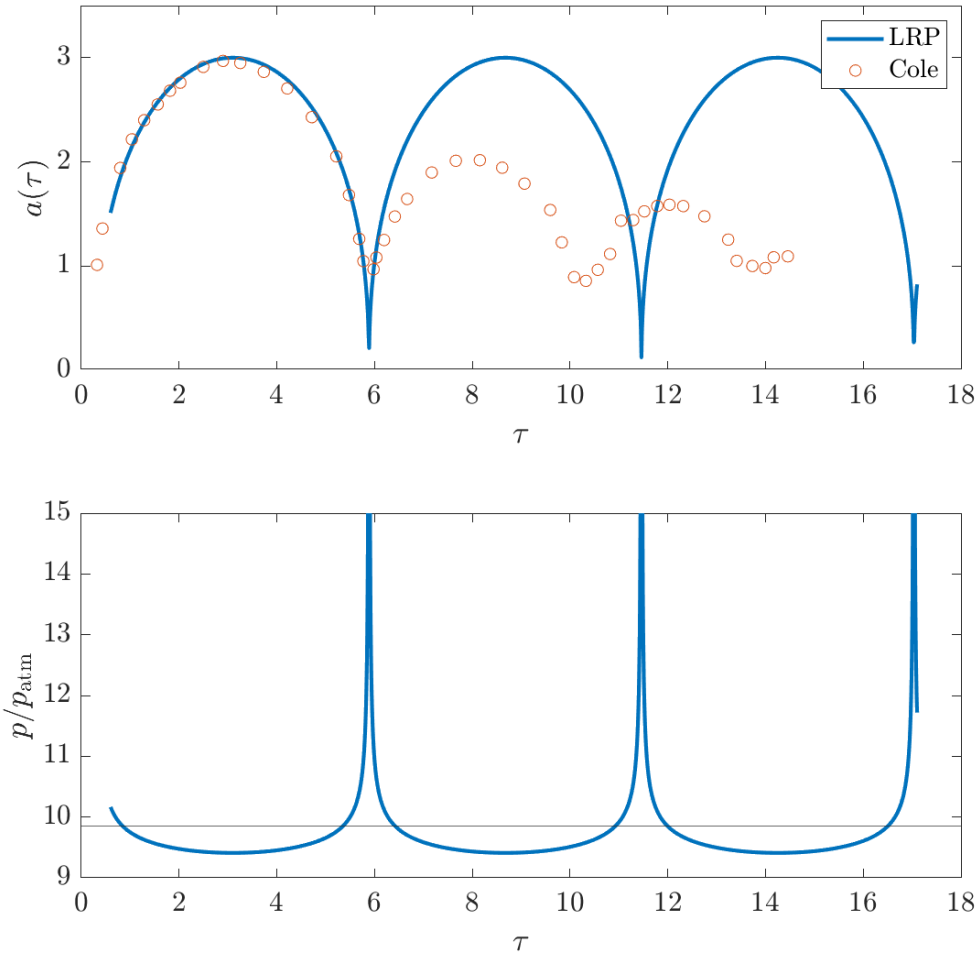

Figure C.1 *The experimental data (Cole) and numerical solution of the dimensionless Lamb–Rayleigh–Plesset (LRP) equation for a 0.25 kg tetryl charge detonated 91.44 m below the water surface. The radius and time scale is set to* $\bar{R} = 0.15\,\mathrm{m}$ *and* $T = 4.80\,\mathrm{ms}$. *The pressure is normalized with respect to the atmospheric pressure* p_{atm}. *The horizontal line corresponds to* $p_\infty = p_{\mathrm{atm}} + \rho g z$.

D Bubble oscillation models including compressibility

Herring model

In the acoustic approximation, the speed of sound in the surrounding water is constant and equal to the undisturbed speed of sound in water $c = c_\infty$. In addition, the variations of the fluid density can be neglected such that $\rho = \rho_\infty$. Including compressibility in this way, yields the Herring equation [26] of the form

$$R\ddot{R}\left(1 - 2\frac{\dot{R}}{c_\infty}\right) + \frac{3}{2}\dot{R}^2\left(1 - \frac{4}{3}\frac{\dot{R}}{c_\infty}\right) = \frac{p_b - p_\infty}{\rho_\infty} + \frac{R}{\rho_\infty c_\infty}\dot{p}_b\left(1 - \frac{\dot{R}}{c_\infty}\right). \tag{D.1}$$

The terms responsible for compressibility effects are proportional to the $1/c_\infty$ factors, and in the limit $c_\infty \to \infty$ we obtain the Lamb–Rayleigh–Plesset equation. The most important effect is the term proportional to $\dot{p}_b$ as it represents the acoustic radiation of energy. The Herring equation was the first successful identification of the acoustic radiation pressure as the principle loss mechanism in underwater explosions. Nevertheless, in his orginal paper, Herring concluded that the acoustic radiation, turbulence, and heat transfer can not alone account for the damping present in experimental data.

Keller–Kolodner model

To numerically demonstrate the damping effect due to finite compressibility we will consider the slightly more recent Keller–Kolodner model [25], whose dimensionless form is

$$(\dot{a} - C)\left(a\ddot{a} + \frac{3}{2}\dot{a}^2 - a^{-3K} + 1\right) - \dot{a}^3 - (3K - 2)\,a^{-3K}\dot{a} - 2\dot{a} = 0. \tag{D.2}$$

The Keller–Kolodner model also utilizes the acoustic approximation[9] and is therefore very similar to the Herring model. In the above, we have introduced the dimensionless sound speed $C = c_\infty\left(\rho_\infty p_\infty^{-1}\right)^{1/2}$. As in the previous section, we wish to compare the dimensionless Keller–Kolodner model with the dimensionless Lamb–Rayleigh–Plesset equation and the experimental data by Cole. Again we use the case of a 0.25 kg tetryl charge detonated 91.44 m below the water surface. To this end we solve Eq. (D.2) numerically by employing the initial conditions

$$a_0 = 3, \quad \dot{a}_0 = 0, \quad K = 1.25, \quad C = 46.5. \tag{D.3}$$

The numerical solution is plotted in Fig. 4.3. In contrast to the Lamb–Rayleigh–Plesset equation, the Keller–Kolodner equation leads to damped oscillations due to the presence of radiation terms. Nevertheless, we observe that the deviations between experiment and theory increases with the number of oscillations.

Gilmore model

We also include the more general Gilmore model [28] which takes the form

$$R\ddot{R}\left(1 - \frac{\dot{R}}{c_b}\right) + \frac{3}{2}\dot{R}^2\left(1 - \frac{\dot{R}}{3c_b}\right) = H\left(1 + \frac{\dot{R}}{c_b}\right) + \frac{R\dot{H}}{c_b}\left(1 - \frac{\dot{R}}{c_b}\right), \tag{D.4}$$

[9] In the acoustic approximation an equation of state is not explicitly utilized. Technically, the Keller–Kolodner equation can be derived from the wave–equation where it is assumed that the speed of sound is a constant parameter. A constant speed of sound corresponds to that the surrounding water obeys the equation of state $p = c^2\rho$.

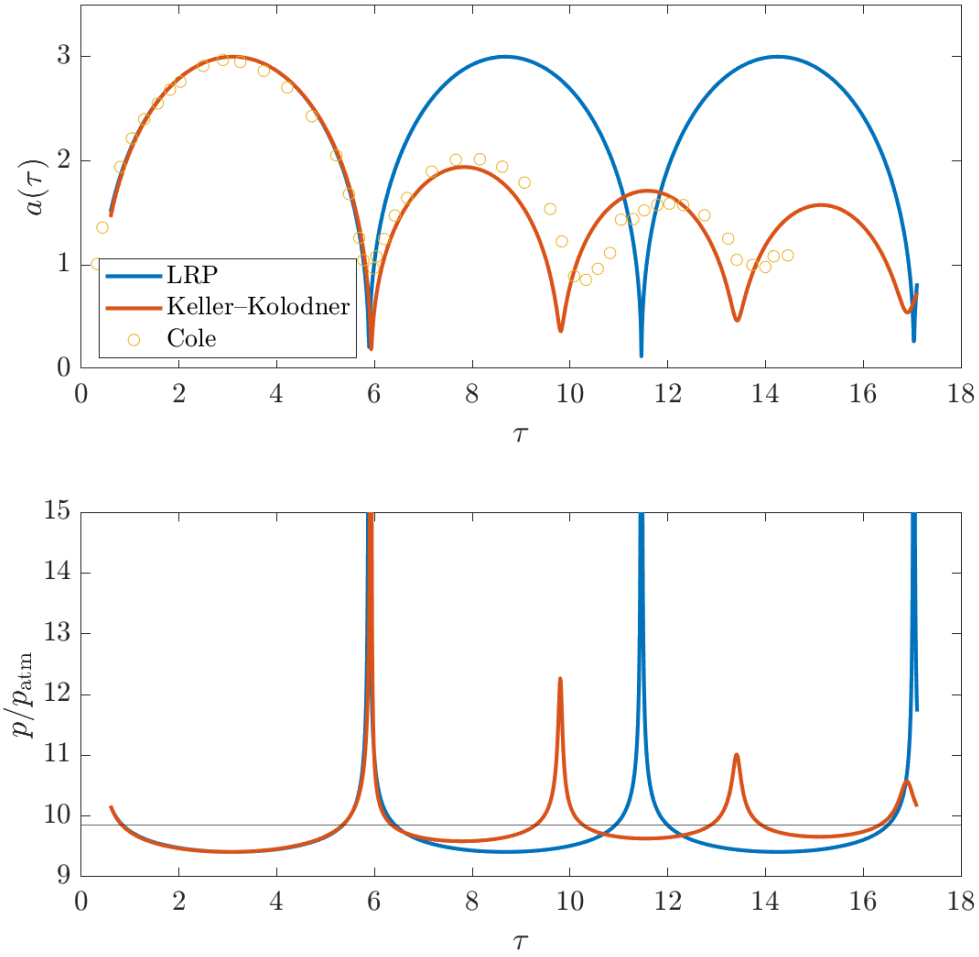

Figure D.1 *The numerical solution of both the Lamb–Rayleigh–Plesset and Keller–Kolodner equation, compared with the experimental data for a 0.25 kg tetryl charge detonated 91.44 m below the water surface. As before the radius and time scale is set to* $\bar{R} = 0.15\,\mathrm{m}$ *and* $T = 4.80\,\mathrm{ms}$. *The pressure is normalized with respect to the atmospheric pressure* p_{atm}. *The horizontal line corresponds to* $p_\infty = p_{\mathrm{atm}} + \rho g z$.

where $c_b = c(p = p_b)$ denotes the speed of sound in the liquid infinitesimally close to the bubble surface. The Gilmore model separates itself from both the Herring and Keller–Kolodner model by explicitly introducing an equation of state for the surrounding water, thereby going beyond the acoustic approximation. Concretely, the modified Tait equation of state

$$\rho(p) = \rho_\infty \left(\frac{p + B}{p_\infty + B} \right)^{\frac{1}{n}} \tag{D.5}$$

is used. The constants B and n depend upon the particular liquid surrounding the gas bubble. For water, $B \approx 3000$ atm and $n \approx 7$. Utilizing the Tait equation of state the speed of sound becomes

$$c = c_\infty \left(\frac{p + B}{p_\infty + B} \right)^{\frac{n-1}{2n}}, \quad c_\infty = \sqrt{n \left(\frac{p_\infty + B}{\rho} \right)}. \tag{D.6}$$

Note that when $p, p_\infty \ll B$ the density and speed of sound approaches their constant values in the undisturbed liquid, and we expect to recover the features of the acoustic approximation. The final ingredient in the Gilmore model is the pressure integral generally defined as

$$H(p_b) = \int_{p_\infty}^{p_b} \frac{\mathrm{d}p}{\rho}. \tag{D.7}$$

For a constant density the pressure integral reduces to the driving term $(p_b - p_\infty)/\rho$ present in the previously discussed models. Physically the pressure integral is identified as the enthalpy difference between the bubble surface and the exterior. Note that in Eq. (D.7) any equation of state can in principle be used. If we utilize the Tait equation of state we obtain

$$H(p_b) = \frac{c^2 - c_\infty^2}{n - 1}. \tag{D.8}$$

Keller–Herring equation

A subtle, but interesting issue with models including compressibility in the acoustic approximation, is that the equations of motion are not unique. In fact, to first order in $1/c_\infty$ it has been demonstrated that a one-parameter family

$$\left[1 + (1 + \Lambda) \frac{\dot{R}}{c_\infty} \right] R\ddot{R} + \frac{3}{2} \left[1 - \left(\Lambda + \frac{1}{3} \right) \frac{\dot{R}}{c_\infty} \right] \dot{R}^2 = \left[1 + (\Lambda - 1) \frac{\dot{R}}{c_\infty} + \frac{R}{c} \frac{\mathrm{d}}{\mathrm{d}t} \right] \frac{p_b - p_\infty}{\rho_\infty} + O\left(c_\infty^{-2} \right) \tag{D.9}$$

of approximate equations for the bubble radius exist. Here Λ is an arbitrary parameter of order 1. Equation (D.9) is called the Keller–Herring equation because it reduces to the form given by each respective author in the limits $\Lambda \to 0$ [25] and $\Lambda \to 1$ [26]. We will not delve further into these issues here, as modern approaches often does not rely on perturbative expansions in $1/c_\infty$. For a deeper explanation and exploration of this subtle issue, as well as higher order generalizations beyond the acoustic approximation, see the articles by Prosperetti and Lezzi [30, 31].

Geers–Hunter model

To the best of my knowledge the most sophisticated semi–empirical model that encapsulates the shock–wave phase, damping, and migration for a spherical bubble is the Geers–Hunter model, originally developed in [32]. The model couples the initial shockwave phase to the bubble oscillation phase, in the sense that the shock wave provides initial conditions for the bubble motion. Furthermore, the model couples the evolution of the bubble radius and vertical migration during the oscillation phase. The model also introduces new damping mechanisms due to wave propagation in the fluid and gas. Concretely, the wave–damping terms are proportional to the radius–dependent impedance ratio

$$\zeta = \frac{\rho_{\text{gas}} c_{\text{gas}}}{\rho_{\text{water}} c_{\text{water}}} \tag{D.10}$$

between the gas bubble and surrounding water. As a consistency check, it has been shown that the Geers–Hunter model reduces to the previously discussed equations of motion (Lamb–Rayleigh–Plesset, Herring, Gilmore, and Keller–Kolodner) by taking the appropriate zero–impedance limits $\left(1/c_{\text{gas}}, c_{\text{water}}, \rho_{\text{water}}/\rho_{\text{gas}} \rightarrow \infty\right)$.

In an improved version of the Geers–Hunter model [59] an attempt is made to also account for bubble distortion on translation and dilation. Concretely, the improvement introduces an artificial bubble drag function of the form $C|v|^P$, where v is the translation velocity, and C and P are parameters that are fit to empirical formulas. The recommended values are $C = 0.4$ and $P = 1$ for charge weights between 45 - 450 kg, and depths exceeding 60 m. Unfortunately, the coupled set of non–linear equations of motion constituting the Geers–Hunter model are far too unwieldy to be included and discussed further in this text. Finally, we note that the improved Geers–Hunter model is the underlying description of the implemented "LOAD_UNDEX" command in Impetus making it particularly useful for benchmarking purposes.

E Kelvin Impulse and bubble–surface interaction

In this chapter we discuss the interaction between a bubble and either rigid or free surfaces. The purpose of this chapter is twofold. Firstly, we want to introduce the interested reader to the physics governing the apparent attractive (repulsive) force experienced by a bubble pulsating in the vicinity of a rigid (free) surface. Secondly, we want to provide the Impetus development team with concrete benchmarks, such that the Impetus code can be developed to incorporate bubble–surface interactions. Consequently, this chapter is slightly more mathematically involved so that hopefully all definitions are unambiguous. As of yet, we point out that the phenomena introduced in this chapter has not been modeled in Impetus.

E.1 Bubble repulsion or attraction

The Kelvin impulse $\mathbf{I}$ of the bubble is defined [33, 34, 35] as

$$\mathbf{I} = \rho \oint_S \phi \mathbf{n} \mathrm{d}S \tag{E.1}$$

where S denotes the bubble surface with the normal vector $\mathbf{n}$, pointing towards the interior of the bubble. The integrand is the velocity potential defined for irrotational[10] flows through the relation $\mathbf{v} = \nabla\phi$.

External forces $\mathbf{F}$ acting on the bubble, will change the Kelvin impulse according to the equation

$$\mathbf{F} = \frac{\mathrm{d}\mathbf{I}}{\mathrm{d}t}, \quad \text{or} \quad \mathbf{I}(t) = \mathbf{I}(0) + \int_0^t \mathbf{F}(\tau)\mathrm{d}\tau. \tag{E.2}$$

For underwater bubbles the external forces are typically caused by gravity, and geometric surfaces (rigid or free) which we denote by ζ. The relevant external forces can be expressed through the velocity potential as

$$\mathbf{F} = \rho \int_\zeta \left\{ \frac{1}{2} |\nabla\phi|^2 \mathbf{n} - (\mathbf{n} \cdot \nabla\phi) \nabla\phi \right\} \mathrm{d}S + \rho \int_V \nabla\Phi \mathrm{d}V, \tag{E.3}$$

where the first and second term represents the Bjerknes force and buoyancy due to gravity respectively. Here V and $\Phi = gz$ denotes the bubble volume and the gravitational potential. The second term trivially becomes the buoyancy force $\rho g V$, while the first term depends on the form of the velocity potential. The velocity potential has to be chosen such that the boundary condition at the relevant surface is satisfied. For a rigid surface the boundary condition is that the velocity should only have a component parallel to the surface, so that the potential should satisfy $\mathbf{n} \cdot \nabla\phi = 0$. For a free surface the appropriate boundary condition is that the velocity is continuous and that pressure should be equal to the atmospheric pressure, in that case the potential should satisfy $\partial\phi/\partial t - (\nabla\phi)^2/2 = 0$. Satisfying the aforementioned boundary conditions can be done in a number of ways, of particular interest is utilizing the method of images. The lowest order approximation of the Kelvin impulse

[10] For the case considered here, we employ the assumption of incompressible flow $\nabla \cdot \mathbf{v} = 0$, such that the velocity potential satisfies the Laplace equation. Consequently, the potentials obey the superposition principle, so that complex flows can be expressed as a sum of simpler flows. The mentioned linearity enables us to utilize the method of images, where surfaces are replaced by appropriate potentials. We also assume the flow to be inviscid, both for simplicity, and to avoid problems with boundary layers close to rigid surfaces.

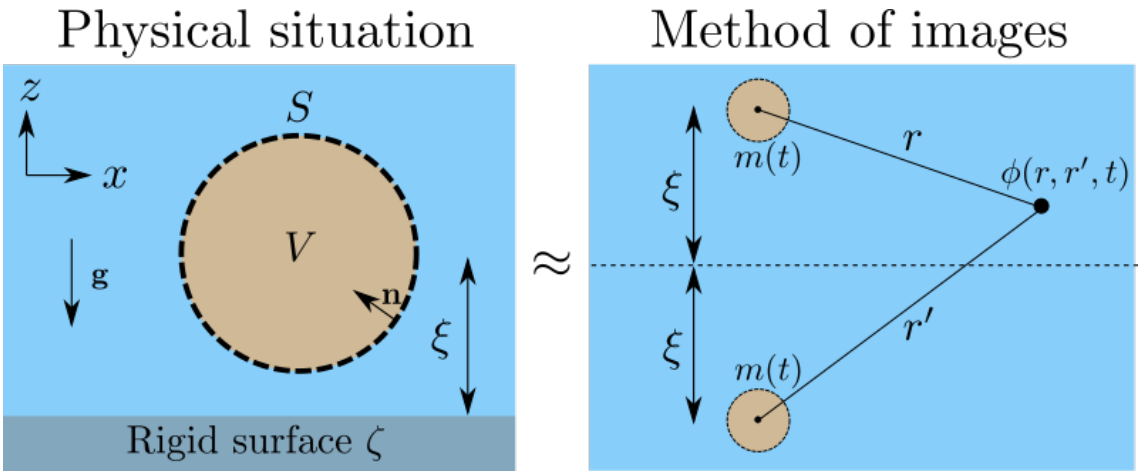

Figure E.1 ***Left:*** *Geometry illustrating the balance between the bubble buoyancy and the Bjerknes attraction to a rigid surface.* ***Right:*** *Strategy of the method of images, where the rigid surface (dashed line) is removed and replaced by an imaginary bubble. The contribution to the total potential is the same when the point of measurement is sufficiently distant from the rigid surface.*

utilizes only time-dependent point sources or sinks, one at the centre of the bubble mimicking bubble pulsation and one at the opposite side of the corresponding surface to fix the correct boundary condition.

A particularly well-known analytical approach is discussed elegantly in [36, 37]. The geometry consists of a bubble located a distance $\xi(t)$ above a horizontal semi-infinite rigid surface, as shown in Fig. E.1. Utilizing the method of images the total velocity potential is given by

$$\phi = -\frac{m(t)}{4\pi r} - \frac{m(t)}{4\pi r'}, \tag{E.4}$$

where r and r' is the distance to a point of measurement from the bubble centroid and image source respectively. The point source strengths are denoted by $m(t)$. The velocity potential in Eq. (E.4) produces an external force of the form

$$F_z = -\frac{\rho m^2(t)}{16\pi\xi^2(t)} + \rho g V(t) \tag{E.5}$$

where there is a competition between the buoyancy and Bjerknes force, trying to force the bubble downwards and upwards respectively. To determine the corresponding impulse, through Eq. (E.2), we further assume that:

1. The bubble retains its spherical form so that $V(t) = 4/3\pi R^3$, and $m(t) = 4\pi R^2 \dot{R}$.
2. The distance between the bubble centroid and rigid surface is constant throughout the motion and equal to its initial value $\xi(t) = \xi_0$.
3. The time dependence of the radius is governed by the Lamb–Rayleigh–Plesset equation

$$m(t) = \pm 4\pi R^2 \left[\frac{2}{3}\left(\frac{\Delta p}{\rho}\right)\left(\frac{R_{\max}^3}{R^3} - 1\right)\right]^{1/2}.$$

The positive (negative) sign is used during the expansion (contraction) phase.

By utilizing the above assumptions and integrating the external force in Eq. (E.5) over the first bubble period T_c we obtain the Kelvin impulse at the end of the collapse

$$I(T_c) = \frac{2\pi\sqrt{6\rho\Delta p}R_{\max}^5}{9\xi_0^2}\left[2\gamma^2\delta^2 B\left(\frac{11}{6},\frac{1}{2}\right) - B\left(\frac{7}{6},\frac{3}{2}\right),\right] \tag{E.6}$$

where $B(x, y)$ is the complete Beta function, and we have defined $\gamma = \xi_0/R_{\max} > 1$ as the dimensionless distance between the bubble and rigid surface. We have also introduced the dimensionless buoyancy parameter as

$$\delta = \sqrt{\frac{\rho g R_{\max}}{\Delta p}} < 1. \tag{E.7}$$

The crucial point is that the direction of the Kelvin impulse at the end of the bubble lifetime determines the direction of the centroid migration and if a jet is formed, the direction of the jet. The competition between the buoyancy force and the attractive Bjerknes interaction leads to a line in the (γ, δ) parameter space where the Kelvin impulse is zero. The null-line is given by

$$\gamma\delta = \left[\frac{B\left(\frac{7}{6},\frac{3}{2}\right)}{2B\left(\frac{11}{6},\frac{1}{2}\right)}\right]^{1/2} \approx 0.442 \tag{E.8}$$

and it partitions the parameter space into one region where the Kelvin impulse is positive (migration away from boundary) and one region where it is negative (migration towards boundary) region.

For a geometry with a free surface above the bubble, the calculation is completely analogous and the final expression for the Kelvin impulse becomes

$$I(T_c) = -\frac{2\pi\sqrt{6\rho\Delta p}R_{\max}^5}{9\xi_0^2}\left[2\gamma^2\delta^2 B\left(\frac{11}{6},\frac{1}{2}\right) - B\left(\frac{7}{6},\frac{3}{2}\right),\right]. \tag{E.9}$$

In the simplest approximation the only difference between a rigid and free surface is a global minus sign in the Kelvin impulse. Therefore, the same partitioning $\gamma\delta \approx 0.442$ exists also for the free surface.

However, for our benchmarking purposes it is more than sufficient to consider the Kelvin impulse formula for a geometry where the rigid surface is inclined by an angle β with respect to the horizontal

$$\frac{\mathbf{I}(T_c)}{\sqrt{\rho\Delta p}R_{\max}^3} = \frac{2\pi\sqrt{6}}{9}\left\{\left[B\left(\frac{7}{6},\frac{3}{2}\right) - \frac{\mu}{2}B\left(\frac{3}{2},\frac{3}{2}\right)\right]\mathbf{\Gamma} + 2\delta^2\left[B\left(\frac{11}{6},\frac{1}{2}\right) + \frac{\mu}{2}B\left(\frac{13}{6},\frac{1}{2}\right)\right]\mathbf{k}\right\}. \tag{E.10}$$

Here the first[11] and second term represents the Bjerknes force due to the rigid surface and buoyancy force respectively. The direction of the Bjerknes force is parallel to the normal vector (pointing away from the bubble) of the rigid surface, and is given by

$$\mathbf{\Gamma} = \frac{1}{\gamma^2}\left(\mathbf{i}\sin\beta - \mathbf{k}\cos\beta\right). \tag{E.11}$$

[11] Note that the term in square brackets, $B\left(\frac{7}{6},\frac{3}{2}\right) - \frac{\mu}{2}B\left(\frac{3}{2},\frac{3}{2}\right)$, is always positive because $\gamma > 1$.

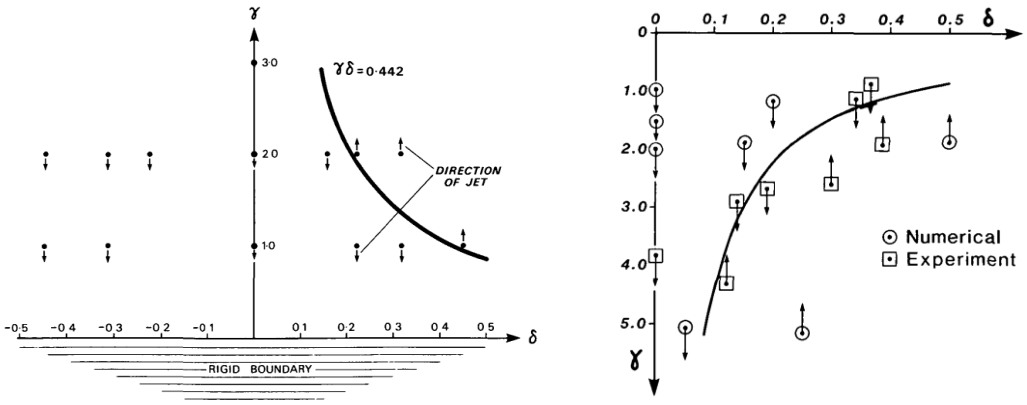

(a) Rigid surface below the bubble. *(b) Free surface above the bubble.*

Figure E.2 The partitioning of the (γ, δ) phase space for (a) a rigid boundary and (b) a free surface. The apparent repulsion or attraction to the surface originates from a competition between the Bjerknes and buoyancy force. The arrows indicate the direction of migration or jet. Figure taken from [35].

The additional terms proportional to $\mu = 1/(2\gamma)$ accounts for a correction to the Rayleigh equation in the presence of a boundary, an effect which was ignored in the simplified derivation given above. To obtain the null-line in Eq. (E.8) one must take the limits $\mu, \beta \to 0$. The corrected null-line is determined from Eq. (E.10) with finite μ and β. A comparison of the simplified and corrected null–line is shown in Fig. E.3. Note that the corrections to the null-line partitioning the parameter space are small and quantitative. The more interesting aspect of Eq. (E.10) is that it can be used to determine the direction of migration for different orientations of the rigid surface, which will be useful in our benchmarking. A concrete example would be to investigate the direction of the bubble migration as a function of the inclination angle of the rigid surface.

E.2 Analogy to electrostatics

Interestingly, we note that the method of images allows for an analogy between bubble interactions and Coloumb's law for electrostatics. Concretely, from the force expressions:

$$F_{\text{Coulomb}} = +\frac{1}{4\pi\epsilon_0}\frac{q_1 q_2}{r^2}, \quad \text{and} \quad F_z = -\frac{1}{4\pi/\rho}\frac{m_1 m_2}{(2\xi)^2}, \tag{E.12}$$

we obtain the correspondence

$$r \leftrightarrow 2\xi, \quad \epsilon_0 \leftrightarrow 1/\rho, \quad q_{1,2} \leftrightarrow m_{1,2}. \tag{E.13}$$

The correspondence tells us that sources pulsating in and out of phase attract and repel respectively. From a fundamental point of view this analogy arises in the lowest order approximation because both phenomena are governed by the Laplace equation. We should be careful in stretching this analogy too far, but it does indicate that two sufficiently spatially separated bubbles either attract or repel depending on the phase difference between them. For a review on the experimental investigation of two–bubble interactions see the papers by Li and Liu [17, 60] and the references therein.

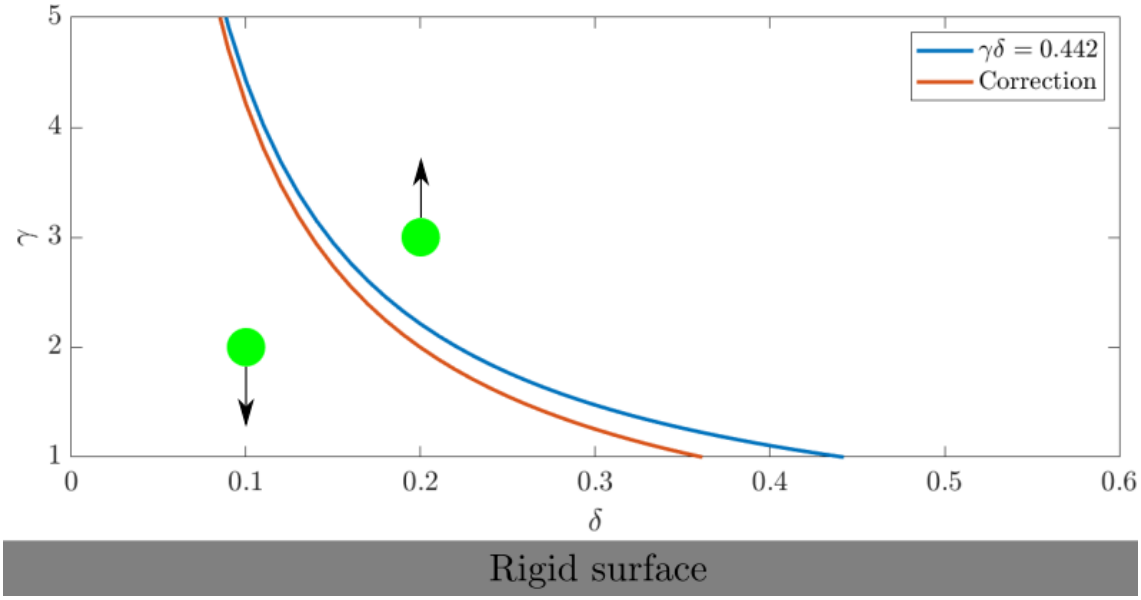

Figure E.3 *The blue line represents $\gamma\delta = 0.442$, the red line represents the full numerical solution of Eq.* (E.10) *for the case $\beta = 0$. Note that the correction to the partition is only quantitative and small.*

E.3 A brief comment on jet–structure interaction

Finally, we will very briefly mention an approximate expression quantifying the interaction between the bubble jet and a solid interface. Since the jet is so thin, a one dimensional description is often sufficient. In general, when a high-speed liquid impacts a target material, a water-hammer pressure is generated and obeys the equation [61, 62]

$$p_{\text{wh}} = \rho_L c_L v_J \frac{\rho_S c_S}{\rho_S c_S + \rho_L c_L}. \tag{E.14}$$

Here $\{c_L, \rho_L\}$, and $\{c_S, \rho_S\}$ are the speed of sound and density of the liquid and target material respectively. The relative impact velocity between the liquid and target material is denoted by v_J. There are then two cases of special interest:

- During jet formation, the high–speed water first impacts the distal side of the bubble. In this case the target material is water moving moving at a velocity v_D. In this case, the relative velocity between the jet and bubble is $|v_J - v_D|$ and $\rho_S c_S = \rho_L c_L$. Thus, the water hammer pressure becomes $p_{\text{wh}} = \rho_L c_L |v_J - v_D|/2$.

- After the jet is formed it may eventually impact on a solid material, for instance steel, and the water hammer pressure is given by (E.14). Often, the target has a much larger impedance than water such that $\rho_S c_S \gg \rho_L c_L$. In this case the water hammer pressure simplifies to $p_{\text{wh}} = \rho_L c_L v_J$. If the jet is moving at a speed with scale of km/s, the water hammer pressure will be on the GPa scale. For comparison this pressure is larger than the pressure of the peak shockwave from the initial explosion.

F Short overview of the boundary integral method

In the simplest possible situation, we make the standard assumptions of irrotational, inviscid, and incompressible flow. Consequently, we can introduce the velocity potential $\mathbf{v} = \nabla\phi$ which satisfies the Laplace equation $\nabla^2\phi = 0$. The solution $\phi(\mathbf{p})$ to the Laplace equation, at a point $\mathbf{p}$ in the fluid domain, can be expressed via the corresponding Green's function G as an integral over the surface boundary $\partial\Omega$ of the fluid volume Ω

$$c(\mathbf{p})\phi(\mathbf{p}) = \int_{\partial\Omega} \left(\frac{\partial\phi}{\partial n} G - \phi \frac{\partial G}{\partial n} \right) \mathrm{d}S, \quad \nabla^2 G(\mathbf{p}, \mathbf{q}) = \delta(\mathbf{p} - \mathbf{q}). \tag{F.1}$$

Here $\partial/\partial n = \mathbf{n} \cdot \nabla$ is the normal derivative at the boundary, $c(\mathbf{p})$ is a geometrical parameter associated with the solid angle, and $\mathbf{q}$ is a point on the bubble surface. For concreteness, we also provide two examples of common Green's functions. For a free–field bubble the fluid domain is infinite and the Green's function is

$$G_\infty = \frac{1}{|\mathbf{p}| - |\mathbf{q}|}. \tag{F.2}$$

In the vicinity of a rigid surface we can employ the method of images. The boundary condition at the surface is fulfilled by placing an image of the bubble at the position $|\mathbf{q}'|$, such that the points $|\mathbf{q}|$ and $|\mathbf{q}'|$ are related by a reflection about the rigid boundary. We then obtain the Green's function

$$G_{\text{rigid surface}} = \frac{1}{|\mathbf{p}| - |\mathbf{q}|} + \frac{1}{|\mathbf{p}| - |\mathbf{q}'|}. \tag{F.3}$$

The integration in Eq. (F.1) has to be performed on all the relevant surfaces. Therefore, we typically only require meshes on the surfaces of the bubble which reduces the dimension of the problem by one. If we know the bubble geometry and the potential at some time, as well as the Green's function, we can solve Eq. (F.1) for the normal fluid velocity $\partial\phi/\partial n$ at the bubble surface. We can then use $\partial\phi/\partial n$ to determine the bubble surface and potential at a later time, and iterate forward in time. The mesh description of the bubble allows us to easily describe non–spherical bubbles and to some extent incorporate bubble interactions with structures. For more details, see the thesis by Best [37].

G Basic interpolant of SPH

To make the idea behind smoothed particle hydrodynamics (SPH) more concrete, we will first derive the basic–interpolant, and then state the relevant equations of motion in the SPH scheme. Formally, we begin by considering an arbitrary local property $A(\mathbf{r})$ (velocity, density, pressure, ...). Through the Dirac function the general property can be expressed as

$$A(\mathbf{r}) = \int A(\mathbf{r}')\delta(\mathbf{r} - \mathbf{r}')\mathrm{d}\mathbf{r}'. \tag{G.1}$$

The underlying idea is now to approximate the Delta function by the so called Kernel function $W(\mathbf{r} - \mathbf{r}'; h)$. Here h represents the width of the Kernel, and a typical choice of Kernel functions are Gaussian or spline functions. The restriction on the Kernel is that in the limit $h \to 0$ it should approach the Delta function. By employing the Kernel, the general property can be expressed as

$$A(\mathbf{r}) \approx \int A(\mathbf{r}')W(\mathbf{r} - \mathbf{r}'; h)\mathrm{d}\mathbf{r}' = \int A(\mathbf{r}')\frac{W(\mathbf{r} - \mathbf{r}'; h)}{\rho(\mathbf{r}')}\rho(\mathbf{r}')\mathrm{d}\mathbf{r}'. \tag{G.2}$$

In the above we introduced the density such that $\rho\mathrm{d}\mathbf{r}$ can be interpreted as an infinitesimal mass element. To proceed we discretize the continuous fluid into N discrete particles labeled by roman letters (a, b, ...). The arbitrary property then takes its final SPH form

$$A_a \approx \sum_{b=1}^{N} A_b \frac{W_{ab} m_b}{\rho_b}. \tag{G.3}$$

The physical interpretation is that at the point of interest $\mathbf{r}$ there is a particle (a), whose properties are determined by the particles (b) surrounding it. The interaction between the particles is given by the Kernel W_{ab}, which decays as the distance between the particles increases. As a simple example, consider the case where the general property is the density at point a, such that

$$\rho_a \approx \sum_b W_{ab} m_b. \tag{G.4}$$

Equation (G.4) states that the density at the point of interest is determined by the mass of the particles surrounding it. Note that the derivative of A is determined by the derivative of the Kernel in its entirety

$$(\nabla A)_a \approx \sum_{b=1}^{N} A_b \frac{m_b}{\rho_b} \nabla_a W_{ab}. \tag{G.5}$$

If $\mathbf{A}$ is a vector property then the divergence of the basic interpolant becomes

$$(\nabla \cdot \mathbf{A})_a \approx \sum_{b=1}^{N} \frac{m_b}{\rho_b} \mathbf{A}_b \cdot \nabla_a W_{ab}. \tag{G.6}$$

By now utilizing Eqs. (G.3), (G.5), and (G.6) the Euler equations, governing inviscid fluid dynamics, can be expressed as

$$\begin{aligned}
\frac{D\rho_a}{Dt} &\approx \rho_a \sum_b \frac{m_b}{\rho_b} \mathbf{v}_{ab} \cdot \nabla_a W_{ab}, \\
\frac{D\mathbf{v}_a}{Dt} &\approx -\sum_b m_b \left(\frac{p_a}{\rho_a^2} + \frac{p_b}{\rho_b^2} \right) \nabla_a W_{ab}, \\
\frac{De_a}{Dt} &\approx -\sum_b m_b \left(\frac{p_a}{\rho_a^2} \mathbf{v}_b + \frac{p_b}{\rho_b^2} \mathbf{v}_a \right) \cdot \nabla_a W_{ab}.
\end{aligned} \tag{G.7}$$

Here e is the sum of the kinetic and internal energy of the fluid. In the presence of viscocity and consequently shear-stresses the Euler equations become the Navier–Stokes equations and the pressure in the equations above become replaced by the stress tensor, as well as the inclusion of shear–strain rate terms.

H Impetus code

H.1 Coupled FE and SPH method

Below we provide an example of the code used to simulate underwater explosions, where the water close to the explosion is discretized into SPH particles and the water far away from the explosion is discretized into a FE mesh, as explained in Sec. 5.2.1.

```
*UNIT_SYSTEM
SI

*PARAMETER
z0 =-350,                       "z-min"
z1 =-300,                       "z-bubble center"
z2 = 0,                         "z-max"
R  = 15,                        "radius of cylindircal hole in mesh"
H  = 40,                        "height of cylindrical hole in mesh"
dx = 3,                         "element size"
tend = 2,                       "Termination time"
num_imp = 100,                  "number of .imp files"
num_ascii = 1000,               "number of .out time steps"
rExplosive = 0.5,               "radius of explosive"
Nt = 2*floor(0.25*pi*%R/%dx)

*TIME
%tend

*OUTPUT
%tend/%num_imp, %tend/%num_ascii

#--- DEFINE WATER MESH ---

*COMPONENT_CYLINDER
1, 1,  [(%z1-%R-%z0)/%dx],  [%Nt]
0, 0, [%z0],  0, 0, [%z1-%R],  [%R]

*COMPONENT_CYLINDER
2, 1,  [(%z2-%H-%z1+%R)/%dx],  [%Nt]
0, 0, [%z1+%H-%R],  0, 0, [%z2],  [%R]

*COMPONENT_PIPE
3, 1,  [(%z1-%R-%z0)/%dx],  [4*%Nt],  [2*%R/%dx]
0, 0, [%z0],  0, 0, [%z1-%R],  [%R], [3*%R]

*COMPONENT_PIPE
4, 1,  [%H/%dx],  [4*%Nt],  [2*%R/%dx]
0, 0, [%z1-%R],  0, 0, [%z1+%H-%R],  [%R], [3*%R]
```

```
*COMPONENT_PIPE
5, 1,  [(%z2-%H-%z1+%R)/%dx],  [4*%Nt],  [2*%R/%dx]
0, 0, [%z1+%H-%R],  0, 0, [%z2],  [%R], [3*%R]

*MERGE_DUPLICATED_NODES
P, 1, P, 1, [%dx/10]

*CHANGE_P-ORDER
P, 1, 3, 123

*GEOMETRY_PIPE
123
0, 0, [%z1-2*%R],  0, 0, [%z1+%H],   [2*%R]

*SMOOTH_MESH
P, 1, 45.0

#--- FLUID PROPERTIES ---

*MAT_FLUID #mid = 1
1, 1000, 2.1e9, 1e-3, 0, 1

*EOS_GRUNEISEN
1, 1.5, 2.0

*MAT_FLUID #mid = 2
2, 1000, 2.1e9, 1e-3
1.0e6

*PART #Combines pid=1 with mid=1 to make a mesh of water.
"Water"
1, 2

#--- DEFINE PARTICLES ---

*PARTICLE_DOMAIN
0, 0, 8.0e6, 0, 1.0e10
[-2*%R], [-2*%R], [%z1-2*%R],  [2*%R], [2*%R], [%z1+%H]

*GEOMETRY_PIPE #gid = 1, to be made into water
1
0, 0, [%z1-%R], 0, 0, [%z1+%H-%R], [%R]

*PARTICLE_SPH  #Particles are made of the material mid=1 (vann)
               #The geometry gid=1 is then discretized into particles
```

```
1
1, 1

*GEOMETRY_SPHERE #gid = 2, to be made into explosive
2
0, 0, [%z1],  [%rExplosive]

*PARTICLE_HE
"TNT" #Particles are made of TNT material
      #The geometry gid=2 is discretized into explosive particles
2, 4
TNT, 2, ,8

*PARTICLE_DETONATION
10
0, 0, [%z1]

# -- GRAVITY INITIALIZATION ---

*LOAD_GRAVITY #Includes gravity in the z-direction
Z, 123

*CURVE
123
0.0, 9.81
1.0, 9.81

*INITIAL_STRESS_FUNCTION #Defines initial hydrostatic load
DP, 1, 222, 222, 222

*INITIAL_STRESS_FUNCTION
P, 1, 222, 222, 222

*FUNCTION
222
9.81*1000*(z)

# --- MERGE PARTICLES AND MESH ---

*MERGE
DP, 1, P, 1

# --- BCs ---

*BC_MOTION
"bottom"
```

```
101
G, 101, Z

*GEOMETRY_SEED_COORDINATE
101
0, 0, [%z0]

*BC_MOTION
"side"
102
G, 102, XY

*GEOMETRY_SEED_COORDINATE
102
[5*%R], 0, [%z1]

*END
```

H.2 Pure SPH method

Below we provide an example of the code used to simulate underwater explosions where the water is only described by SPH particles, as explained in Sec. 5.2.2. In short, the explosive is surrounded by different water geometries with individual particle densities. The particle density in a layer close to the explosive is larger than in a layer far away from the explosive.

```
*UNIT_SYSTEM
SI

*PARAMETER
z1         = -50            , "z-bubble center"
tend       = 2              , "termination time"
num_imp    = 100            , "number of .imp files"
num_ascii  = 1000           , "number of .out time steps"
rExplosive = 0.5            , "radius of explosive charge"
L          = 100            , "total domain size"
rho        = 1000.0         , "Density of water"
bulk       = 2.1e9          , "Bulk modulus of water"
g          = 9.81           , "Acceleration of gravity"

*TIME
%tend

*OUTPUT
%tend/%num_imp, %tend/%num_ascii

#--- FLUID PROPERTIES (Same result if EOS is not used) ---
```

```
*MAT_FLUID
1, [%rho], [%bulk], 1e-3, 0, 1
*EOS_GRUNEISEN
1, 1.5, 2.0

#--- FLUID GEOMETRY ---

*PARTICLE_DOMAIN #Define particle domain and BCs
, , 1.0e7
[-%L], [-%L], [-%L/2], [%L], [%L], [%L]
2, 2, 2, 2, 2, 2

*GEOMETRY_BOX  #Geometry of 1st water layer
"Water L1"
1
[-%L], [-%L], [-%L/2], [%L], [%L], [%L/2]

*PARTICLE_SPH  #Discretizes the geometry above into water particles
"Water L1"
1
1, 1, 0, 0, 0.01

*GEOMETRY_BOX  #Geometry of 2nd water layer
"Water L2"
2
[-%L/2], [-%L/2], [-%L/2], [%L/2], [%L/2], [%L/2]

*PARTICLE_SPH  #Discretizes the geometry above into water particles
"Water L2"
2
1, 2, 0, 0, 0.02

*GEOMETRY_SPHERE  #Geometry of 3rd water layer
"Water L3"
3
0, 0, 0, [40]

*PARTICLE_SPH  #Discretizes the geometry above into water particles
"Water L3"
3
1, 3, 0, 0, 0.04

*GEOMETRY_SPHERE  #Geometry of 4th water layer
"Water L4"
4
```

```
0, 0, 0, [35]

*PARTICLE_SPH  #Discretizes the geometry above into water particles
"Water L4"
4
1, 4, 0, 0, 0.08

*GEOMETRY_SPHERE  #Geometry of 5th water layer
"Water L5"
5
0, 0, 0, [30]
*PARTICLE_SPH  #Discretizes the geometry above into water particles
"Water L5"
5
1, 5, 0, 0, 0.16

*GEOMETRY_SPHERE  #Geometry of 6th water layer
"Water L6"
6
0, 0, 0, [25]

*PARTICLE_SPH  #Discretizes the geometry above into water particles
"Water L6"
6
1, 6, 0, 0, 0.32

*GEOMETRY_SPHERE  #Geometry of TNT layer
"TNT"
7
0, 0, 0, [%rExplosive]

*PARTICLE_HE  #Discretizes the TNT geometry into TNT particles
"TNT"
7, 4
TNT, 7, , 10

*PARTICLE_DETONATION  #Detonation point
10
0, 0, 0

#--- GRAVITY INITIALIZATION ---

*LOAD_GRAVITY
Z, 123

*CURVE
```

```
123
0.0, 9.81
1.0, 9.81

*INITIAL_STRESS_FUNCTION  #Loads initial hydrostatic pressure load on L1
DP, 1, 222, 222, 222

*INITIAL_STRESS_FUNCTION  #Loads initial hydrostatic pressure load on L2
DP, 2, 222, 222, 222

*INITIAL_STRESS_FUNCTION  #Loads initial hydrostatic pressure load on L3
DP, 3, 222, 222, 222

*INITIAL_STRESS_FUNCTION  #Loads initial hydrostatic pressure load on L4
DP, 4, 222, 222, 222

*INITIAL_STRESS_FUNCTION  #Loads initial hydrostatic pressure load on L5
DP, 5, 222, 222, 222

*INITIAL_STRESS_FUNCTION  #Loads initial hydrostatic pressure load on L6
DP, 6, 222, 222, 222

*FUNCTION  #Function defining hydrostatic pressure load
222
-101325 - %g*%rho*(%L/2 - z)

*END
```

H.3 Shockwave propagation

Below we provide an example of the code used to simulate the shockwave propagation resulting from an underwater explosions, as explained in Sec. 5.3.

```
*UNIT_SYSTEM
SI

*PARAMETER
z1         =-50,"z-bubble center"
tend       = 60*0.001,"termination time"
num_imp    = 100,"number of .imp files"
num_ascii  = 1000,"number of .out time steps"
rExplosive = 0.5,"radius of explosive charge"
L          = 100,"total domain size"
rho        = 1000.0 "density of water"
bulk       = 2.1e9 "bulk modulus of water"
g          = 9.81 "acceleration of gravity"
```

```
*TIME
%tend

*OUTPUT
%tend/%num_imp, %tend/%num_ascii

*OUTPUT_SENSOR #Placing pressure sensors
"5m"
1, SPH,  5, 0, 0
"10m"
2, SPH, 10, 0, 0
"15m"
3, SPH, 15, 0, 0
"20m"
4, SPH, 20, 0, 0

#--- FLUID PROPERTIES (Same result if EOS is not used) ---
*MAT_FLUID #mid = 1
1, [%rho], [%bulk], 1e-3, 0, 1

*EOS_GRUNEISEN
1, 1.5, 2.0

*PARTICLE_DOMAIN #Define particle domain and BCs
0, 0, 2.0e7
~if %L/2+%z1 < 0
  [-%L/2], [-%L/2], [-%L/2],  [%L/2], [%L/2], [%L/2]
  2, 2, 2,  2, 2, 2
~else
  [-%L/2], [-%L/2], [-%L/2],  [%L/2], [%L/2], [%L/2+1]
  2, 2, 2,  2, 2, 0
~end_if

#--- FLUID GEOMETRY---
*GEOMETRY_BOX
"Water L1"
1
[-%L/2], [-%L/2], [-%L/2],  [%L/2], [%L/2], [min(%L/2,-%z1)]

*PARTICLE_SPH
"Water L1"
1
1, 1, 0, 0, 0.01


*GEOMETRY_BOX
```

```
"Water L2"
2
[-%L/4], [-%L/4], [-%L/4],  [%L/4], [%L/4], [min(%L/4,-%z1)]

*PARTICLE_SPH
"Water L2"
2
1, 2, 0, 0, 0.02

*GEOMETRY_SPHERE
"Water L3"
3
0, 0, 0,  [24]

*PARTICLE_SPH
"Water L3"
3
1, 3, 0, 0, 0.04

*GEOMETRY_SPHERE
"Water L4"
4
0, 0, 0,  [17]

*PARTICLE_SPH
"Water L4"
4
1, 4, 0, 0, 0.08

*GEOMETRY_SPHERE
"Water L5"
5
0, 0, 0,  [12]

*PARTICLE_SPH
"Water L5"
5
1, 5, 0, 0, 0.16

*GEOMETRY_SPHERE
"Water L6"
6
0, 0, 0,  [7]

*PARTICLE_SPH
"Water L6"
```

```
6
1, 6, 0, 0, 0.32

*GEOMETRY_SPHERE
"TNT"
7
0, 0, 0,  [%rExplosive]

*PARTICLE_HE
"TNT"
7, 4
TNT, 7

*PARTICLE_DETONATION #detoneres i et punkt (x1,y1,z1)
10
0, 0, 0

#--- GRAVITY INITIALIZATION ---
*LOAD_GRAVITY #Includes gravity in the z-direction
Z, 123

*CURVE
123
0.0, 9.81
1.0, 9.81

#--- INITIAL HYDROSTATIC PRESSURE LOAD---
*INITIAL_STRESS_FUNCTION
DP, 1, 222, 222, 222
*INITIAL_STRESS_FUNCTION
DP, 2, 222, 222, 222
*INITIAL_STRESS_FUNCTION
DP, 3, 222, 222, 222
*INITIAL_STRESS_FUNCTION
DP, 4, 222, 222, 222
*INITIAL_STRESS_FUNCTION
DP, 5, 222, 222, 222
*INITIAL_STRESS_FUNCTION
DP, 6, 222, 222, 222

*FUNCTION
222
%g*%rho*(z+%z1)
*END
```

About FFI

The Norwegian Defence Research Establishment (FFI) was founded 11th of April 1946. It is organised as an administrative agency subordinate to the Ministry of Defence.

FFI's mission

FFI is the prime institution responsible for defence related research in Norway. Its principal mission is to carry out research and development to meet the requirements of the Armed Forces. FFI has the role of chief adviser to the political and military leadership. In particular, the institute shall focus on aspects of the development in science and technology that can influence our security policy or defence planning.

FFI's vision

FFI turns knowledge and ideas into an efficient defence.

FFI's characteristics

Creative, daring, broad-minded and responsible.

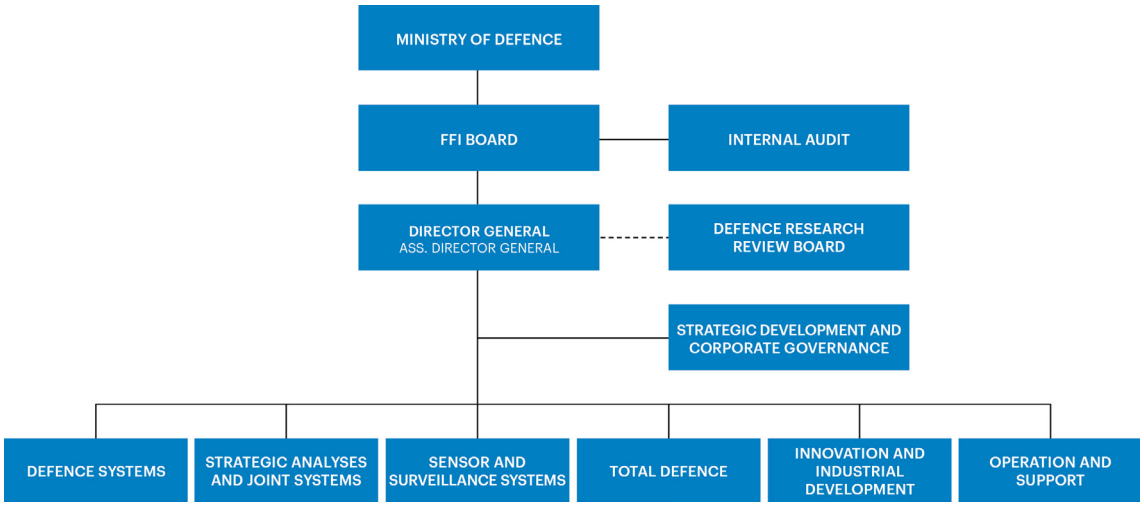

Forsvarets forskningsinstitutt (FFI)
Postboks 25
2027 Kjeller

Besøksadresse:
Kjeller: Instituttveien 20, Kjeller
Horten: Nedre vei 16, Karljohansvern, Horten

Telefon: 91 50 30 03
E-post: post@ffi.no
ffi.no

Norwegian Defence Research Establishment (FFI)
PO box 25
NO-2027 Kjeller
NORWAY

Visitor address:
Kjeller: Instituttveien 20, Kjeller
Horten: Nedre vei 16, Karljohansvern, Horten

Telephone: +47 91 50 30 03
E-mail: post@ffi.no
ffi.no/en